Seismic velocity characterisation of geothermal reservoir rocks for CO_2 storage performance assessment

Janssen, Martijn T.G.; Barnhoorn, Auke; Draganov, Deyan; Wolf, Karl Heinz A.A.; Durucan, Sevket

DOI
10.3390/app11083641

Publication date
2021

Document Version
Final published version

Published in
Applied Sciences (Switzerland)

applied sciences

MDPI

Article

Seismic Velocity Characterisation of Geothermal Reservoir Rocks for CO_2 Storage Performance Assessment

Martijn T. G. Janssen [1,*], Auke Barnhoorn [1], Deyan Draganov [1], Karl-Heinz A. A. Wolf [1] and Sevket Durucan [2]

[1] Department of Geoscience and Engineering, Faculty of Civil Engineering and Geosciences, Delft University of Technology, 2628 CN Delft, The Netherlands; Auke.Barnhoorn@tudelft.nl (A.B.); D.S.Draganov@tudelft.nl (D.D.); K.H.A.A.Wolf@tudelft.nl (K.-H.A.A.W.)

[2] Department of Earth Science and Engineering, Royal School of Mines, Imperial College London, London SW7 2AZ, UK; s.durucan@imperial.ac.uk

* Correspondence: M.T.G.Janssen@tudelft.nl; Tel.: +31-152781704

Abstract: As part of a seismic monitoring project in a geothermal field, where the feasibility of re-injection and storage of produced CO_2 is being investigated, a P- and S-wave seismic velocity characterisation study was carried out. The effect of axial (up to 95 MPa) and radial (up to 60 MPa) stress on the seismic velocity was studied in the laboratory for a broad range of dry sedimentary and metamorphic rocks that make up the Kızıldere geothermal system in Turkey. Thin section texture analyses conducted on the main reservoir formations, i.e., marble and calcschist, confirm the importance of the presence of fractures in the reservoir: 2D permeability increases roughly by a factor 10 when fractures are present. Controlled acoustic-assisted unconfined and confined compressive strength experiments revealed the stress-dependence of seismic velocities related to the several rock formations. For each test performed, a sharp increase in velocity was observed at relatively low absolute stress levels, as a result of the closure of microcracks, yielding an increased mineral-to-mineral contact area, thus velocity. A change in radial stress appeared to have a negligible impact on the resulting P-wave velocity, as long as it exceeds atmospheric pressure. The bulk of the rock formations studied showed reducing P-wave velocities as function of increasing temperature due to thermal expansion of the constituting minerals. This effect was most profound for the marble and calcschist samples investigated.

Keywords: acoustic measurements; seismic velocity characterisation; geothermal reservoir; CO_2 storage; seismic monitoring

Citation: Janssen, M.T.G.; Barnhoorn, A.; Draganov, D.; Wolf, K.-H.A.A.; Durucan, S. Seismic Velocity Characterisation of Geothermal Reservoir Rocks for CO_2 Storage Performance Assessment. *Appl. Sci.* **2021**, *11*, 3641. https://doi.org/10.3390/app11083641

Academic Editor: Jun Matsushima

Received: 30 March 2021
Accepted: 16 April 2021
Published: 18 April 2021

1. Introduction

The total worldwide installed geothermal capacity in 2019 was 15,406 MWe. At the time, the European installed geothermal capacity reached 2960 MWe. The main European players in this field are Italy, Iceland, Turkey, Germany, France, and Portugal, with known and excellent capacities in Hungary, Poland, Romania, and Switzerland [1,2]. With the new plants introduced in 2018, the installed geothermal capacity in Turkey has increased to about 1500 MWe, mainly in the Denizli and Aydin provinces [2–4]. The bulk of the aforementioned installed capacity in Turkey is represented by power plants located along the Büyük Menderes graben.

Although it is widely assumed that geothermal energy is a clean, i.e., zero-emission and renewable energy [5,6], most geothermal energy plants emit carbon dioxide (CO2) as a part of the produced steam. In Turkey, the non-condensable gases that are released from geothermal plants within the country consist of 95 to 98% of CO_2. This leads to total CO_2 emissions from geothermal power plants of roughly 900 to 1300 gr/kWh [7]. The main reason for this is that nearly all geothermal reservoirs in Turkey are producing from carbonate rocks.

The study presented here is part of the ACT2 CCS SUCCEED project where the aim is to investigate, and demonstrate, the feasibility of utilising produced CO_2 for re-injection in a geothermal field. The overall goal of the project is to provide the geothermal energy sector with the means to address the climate change challenge through CO_2 utilisation, to enhance reservoir pressure for geothermal deployment, as well as permanently storing the injected CO_2. This study focusses on one active geothermal power generation site: Kızıldere in Turkey. An existing well will be used to inject both produced and captured CO_2, in supercritical state, into the geothermal reservoir. The idea of combining CO_2 storage with geothermal energy is not new [8–14], and the approach shows similarities with the concept of a CO_2-plume geothermal (CPG) system, proposed by Randolph and Saar [15,16]. Key difference is that in a CPG system, CO_2 is treated as the working fluid, providing energy for electricity generation [15–19], whereas in our approach produced CO_2 is utilised for re-injection to maintain and enhance reservoir pressure as the driving mechanism, and, thus, improving geothermal performance. This provides a cost-effective and low-environmental impact coupled geothermal-CO_2 storage technology.

This study presents an extensive and detailed laboratory investigation for which the reservoir and CO_2 injection conditions that prevail at the Kızıldere site are mimicked. Using reference samples from the geothermal reservoir, acoustic measurements are carried out at varying stresses and temperatures to obtain a baseline seismic-response characterisation. Subsequently, in a later phase of the project, the acquired acoustic data will serve as an input for simulating seismic wave propagation using a detailed subsurface model that represents the Kızıldere site. The simulation results will help the design of the active seismic surveys for the monitoring of CO2 injection performance.

Acoustic wave velocities in different rock types as a function of confining pressure [20–23], pore-pressure [23–26], and temperature [27–32], were studied by many researchers in the past. Bulk of these studies were either done on sedimentary rocks [20,21,26], igneous rocks [23], or on a combination of both [22,24]. Most laboratory studies, aiming at investigating temperature-dependent velocities, were conducted under extremely high pressures (up to 600 MPa) and temperatures (up to 1000 °C). Few researchers have assessed the effect of temperature on seismic velocity in a more realistic range, for geothermal reservoirs of up to 250 °C, utilising saturated samples [31,32].

This study covers a novel comprehensive laboratory investigation on the effects of both axial (up to 95 MPa) and radial (up to 60 MPa) stress on the compressional and shear wave velocities for a wide range of dry sedimentary and metamorphic rocks found at the Kızıldere geothermal reservoir. Additionally, the effect of temperature (up to 240 °C), at atmospheric pressure conditions, for the complete set of rock types, is assessed as well. This led to a unique set of experimental data and corresponding analyses.

2. Materials and Methods

2.1. Sample Collection

The Kızıldere geothermal field covers an area between the provinces of Denizli and Aydin, located in the north-eastern region of the Büyük Menderes Graben, southwest Turkey [33–35]. A high heat flow within this region, which is a consequence of the extensional tectonic regime, produces reservoir temperatures of up to 240 °C at depths below 1200 m [33,36]. The geothermal fluid consists of meteoric water that circulates in fracture systems within the high heat flow regime. A conceptual model of the Kızıldere field is shown in Figure 1.

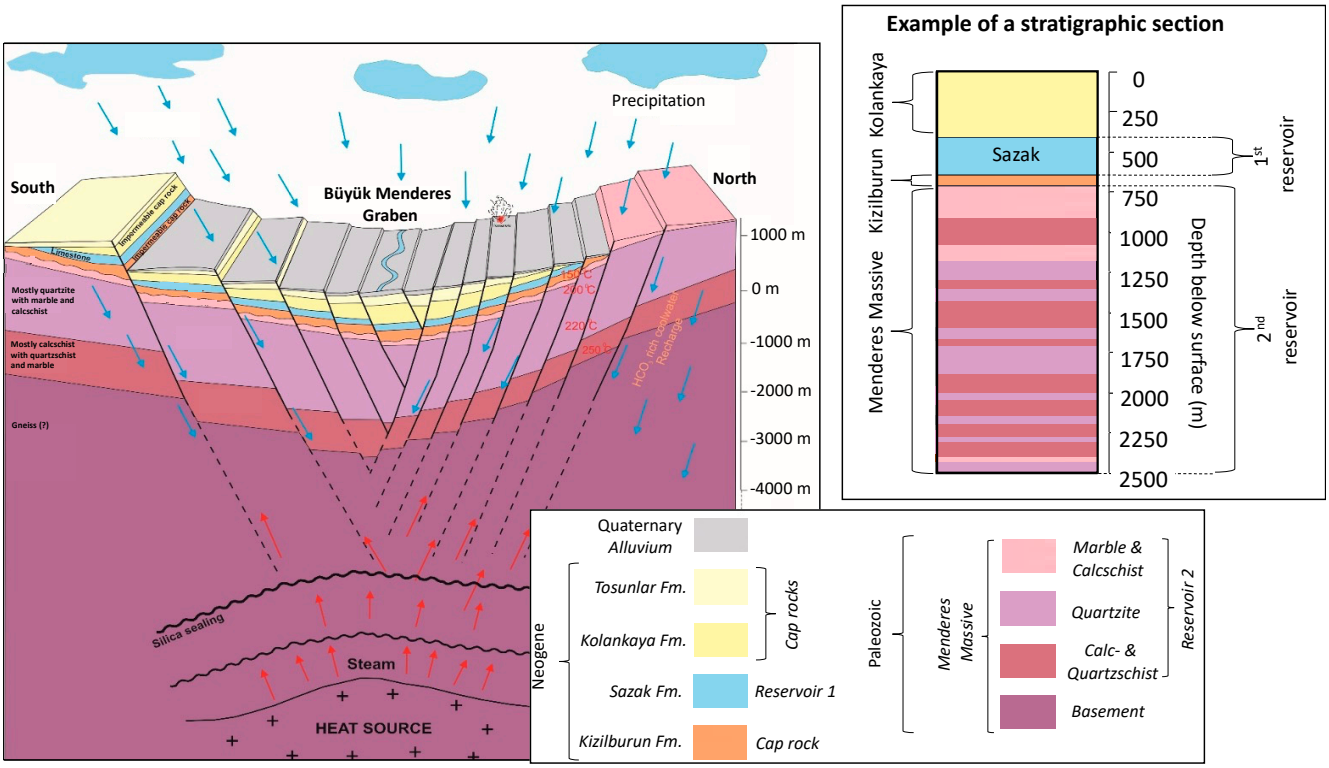

Figure 1. Left: Kızıldere geothermal field conceptual model using the most recent reservoir classification (revised after [33]). Right: Example of a stratigraphic section, revealing the actual formation sequence represented by the three different lithologies that make up the second reservoir.

Multiple rock samples were collected from various fresh outcrops in the region around the Kızıldere site. These included limestone, calcschist, marble, quartzite, siltstone, quartzschist, mudstone, and micaschist. These rock samples represent different lithologies present in the geothermal system (Table 1). Rather than being distinctly stratified as illustrated in the large-scale conceptual model shown in Figure 1, the formation sequence of different lithologies, comprising marble and calcschist, calc- and quartzschist, and quartzite (stratigraphic section in Figure 1), form the second reservoir at Kızıldere. Local layers of micaschists do occur within the calc- and quartzschist intervals.

Table 1. Rock types collected from fresh outcrops in the region around the Kızıldere site.

Rock Type	Formation	Type
Limestone	Sazak	First reservoir
Siltstone	Kızılburun	Regional caprock for second reservoir
Mudstone	Kızılburun	Regional caprock for second reservoir
Marble	Menderes Massive	Part of second reservoir
Quartzite	Menderes Massive	Part of second reservoir
Quartzschist	Menderes Massive	Part of second reservoir
Micaschist	Menderes Massive	Local seal within second reservoir
Calcschist	Menderes Massive	Part of second reservoir

2.2. Core Samples

Multiple cores were drilled from the collected reservoir and caprock samples for the studied geothermal system (Table 1). After drilling, they were cut and dried for 24 h in an oven at 60 °C. Prior to performing the seismic-response characterisation experiments, first the physical properties (i.e., porosity, matrix, and bulk density) of each of the cores were determined. Porosities and matrix densities were measured using an Ultra Pycnometer 1000

(Quantachrome Corporation). All cores have lengths and diameters of 60.8 ± 5.1 mm and 29.7 ± 0.2 mm, respectively. Each core was drilled perpendicular to any potential layering.

Tables 2–5 present an overview of the physical properties of each of the cores used in this study. Several types of dry acoustic-assisted experiments were conducted, ranging from unconfined compressive strength (UCS) tests, where an increasing axial stress (σ_1) was applied on the sample without any confining, i.e., radial, stress ($\sigma_2 = \sigma_3$) applied to it, to confined compressive strength (CCS) experiments, where both σ_1 and σ_2 (=σ_3) were applied on the core samples. Note that throughout this manuscript radial stress is shown as σ_2. Experimental series A, B, C, and D refer to UCS tests, CCS tests with σ_1 equal to σ_2, CCS tests with differential stress ($\sigma_{diff} = \sigma_1 - \sigma_2$) fixed at 45 MPa or 10 MPa, and CCS tests with a constant σ_2 and varying σ_1 (both set at field-representative stresses), respectively. Table S1 (Supplementary Materials) presents the averaged properties per rock type.

2.3. Thin Section Analyses

For several of the rock types presented in Table 1, thin sections, with a thickness of 30 µm, were prepared in the aid of mineralogy and 2D porosity and permeability analyses. For this purpose, a Leitz Laborlux 11 pol S. microscope (Ernst Leitz GmbH) was used. Mineral occurrence and composition were assessed based on random image point counting using 10× and 40× objectives. To obtain the 2D permeability, Carman-Kozeny's equation was used [37,38]. The image analysis was done within an identified area of interest that excludes the edges of the thin sections.

2.4. Experimental Procedure: UCS and CCS Tests

In experimental series A, i.e., the UCS experiments combined with acoustic measurements (Table 2), the effect of increasing σ_1 on the seismic velocities as well as the mechanical behaviour (e.g., static elastic properties) of the various rock samples were studied. The samples were placed inside a uniaxial loading apparatus with a 500 kN loading frame. A hydraulic ram was used to provide and control σ_1. Axial and radial strain were recorded by two linear variable displacement transformers (LVDTs) and an extensometer chain, respectively. All rock samples were deformed until they reached their respective ultimate strengths (i.e., the maximum σ_1 that the sample can withstand before it breaks or weakens). Active-source acoustic measurements were taken during the course of the experiments. The variable in all UCS tests conducted is the axial stress, which was increased using a constant axial displacement rate of 0.0005 mm/s until rock failure occurred.

During the course of experimental series B, C, and D, i.e., the CCS tests combined with active-source acoustic measurements, the effect of both σ_1 and σ_2 on the seismic velocities was investigated. Here, the rock samples were positioned in a Hoek cell [39], which allows one to apply a certain confining pressure (i.e., σ_2) on the sample, before being placed on the abovementioned 500 kN loading frame. The hydraulic ram controlled σ_1 whereas an ISCO pump was used for regulating the confining pressure. Axial strain is again recorded by the two LVDTs. During the experiments active-source acoustic measurements were taken, where attention was paid to how the seismic signal varies as a function of σ_1 and σ_2; reflecting various locations within the subsurface at the Kızıldere reservoir.

Table 2. Properties of the core samples used in experimental series A: UCS tests.

UCS	**Experiment**													
Type	Calcschist		Marble			Limestone			Quartzite			Siltstone		Quartzschist	Mudstone
Code	TD12- CS4	TD12- CS5	TD1- M2	TD1- M3	TS2- SZL2	TS2- SZL4	TS2- SZL5	TD20- QZ-1	TD20- QZ-2	TD20- QZ-4	TK- B1-2	TK- B1-3	TD-23-QMS1	TK-B2-1
Length (mm)	61.6 ± 0.1	61.5 ± 0.1	62.9 ± 0.1	61.9 ± 0.1	58.9 ± 0.1	60.8 ± 0.1	61.4 ± 0.1	62.8 ± 0.1	62.5 ± 0.1	60.8 ± 0.1	62.7 ± 0.1	60.6 ± 0.1	62.5 ± 0.1	63.7 ± 0.1
Diameter (mm)	29.8 ± 0.1	29.8 ± 0.1	29.8 ± 0.1	29.8 ± 0.1	29.1 ± 0.1	29.8 ± 0.1	29.0 ± 0.1	29.8 ± 0.1	29.8 ± 0.1	29.8 ± 0.1	29.8 ± 0.1	29.7 ± 0.1	29.6 ± 0.1	29.7 ± 0.1
Porosity (%)	4.14 ± 0.10	2.42 ± 0.03	3.01 ± 0.13	2.27 ± 0.03	5.33 ± 0.13	10.48 ± 0.24	7.54 ± 0.16	2.77 ± 0.16	2.57 ± 0.03	3.65 ± 0.05	22.55 ± 0.01	25.08 ± 0.08	1.71 ± 0.29	16.60 ± 0.15
Porosity at failure point (%) [a]	5.93 ± 0.10	-	-	4.20 ± 0.07	-	-	-	-	-	4.21 ± 0.03	-	-	-	-
Gas permeability (mD) [b]	-	-	-	-	-	-	-	-	-	-	97 ± 6	-	-	-
Pore Volume (mm^3)	1779 ± 58	1038 ± 22	1321 ± 68	980 ± 21	2088 ± 69	4444 ± 140	3058 ± 92	1213 ± 81	1120 ± 23	1548 ± 34	9861 ± 87	10529 ± 123	735 ± 132	7326 ± 127
Matrix density (g/cm^3)	2.78 ± 0.01	2.75 ± 0.01	2.76 ± 0.01	2.75 ± 0.01	2.73 ± 0.01	2.75 ± 0.01	2.75 ± 0.01	2.89 ± 0.01	2.90 ± 0.01	2.92 ± 0.01	2.78 ± 0.01	2.79 ± 0.01	2.80 ± 0.01	2.82 ± 0.01
Bulk density (g/cm^3)	2.67 ± 0.02	2.68 ± 0.02	2.68 ± 0.02	2.69 ± 0.03	2.59 ± 0.03	2.47 ± 0.03	2.55 ± 0.03	2.81 ± 0.02	2.82 ± 0.02	2.82 ± 0.03	2.15 ± 0.01	2.09 ± 0.02	2.76 ± 0.03	2.36 ± 0.02

[a] Porosity at failure point represents the total porosity at rock failure, i.e., at the end of an UCS test. [b] Gas permeability measured using a Ruska gas permeameter (Ruska Instrument Corporation) could only be measured for the siltstone sample due to limitations of the apparatus (sample porosity has to be sufficiently high) and core availability.

Table 3. Properties of the core samples used in experimental series B: CCS tests ($\sigma_1 = \sigma_2$).

CCS ($\sigma_1 = \sigma_2$)	**Experiment**							
Type	Calcschist	Marble	Limestone	Quartzite	Siltstone	Quartzschist	Mudstone	Micaschist
Code	TD12-CS5	TD1-M1	TS2-SZL4	TD20-QZ-1	TK-B1-2	TD-23-QMS1	TK-B2-1	TD-25-MS-1
Length (mm)	61.5 ± 0.1	60.5 ± 0.1	60.8 ± 0.1	62.8 ± 0.1	62.7 ± 0.1	62.5 ± 0.1	63.7 ± 0.1	41.0 ± 0.1
Diameter (mm)	29.8 ± 0.1	29.8 ± 0.1	29.8 ± 0.1	29.8 ± 0.1	29.8 ± 0.1	29.6 ± 0.1	29.7 ± 0.1	29.7 ± 0.1
Porosity (%)	2.42 ± 0.03	2.67 ± 0.06	10.48 ± 0.24	2.77 ± 0.16	22.55 ± 0.01	1.71 ± 0.29	16.60 ± 0.15	8.52 ± 0.37
Permeability (mD)	-	-	-	-	97 ± 6	-	-	-
Pore Volume (mm^3)	1038 ± 22	1127 ± 35	4444 ± 140	1213 ± 81	9861 ± 87	735 ± 132	7326 ± 127	2420 ± 128
Matrix density (g/cm^3)	2.75 ± 0.01	2.74 ± 0.01	2.75 ± 0.01	2.89 ± 0.01	2.78 ± 0.01	2.80 ± 0.01	2.82 ± 0.01	2.92 ± 0.01
Bulk density (g/cm^3)	2.68 ± 0.02	2.67 ± 0.02	2.47 ± 0.03	2.81 ± 0.02	2.15 ± 0.01	2.76 ± 0.03	2.36 ± 0.02	2.67 ± 0.02
$\sigma_1 = \sigma_2$ (MPa)	5–60	5–60	5–60	5–60	5–60	5–60	5–60	5–60

Table 4. Properties of the core samples used in experimental series C: CCS tests (fixed σ_{diff}).

CCS (Fixed σ_{diff})	**Experiment**						
Type	Calcschist	Marble	Limestone	Quartzite	Siltstone	Quartzschist	Mudstone
Code	TD12-CS5	TD1-M4	TS2-SZL4	TD20-QZ-2	TK-B1-1	TD-23-QMS1	TK-B2-1
Length (mm)	61.5 ± 0.1	62.5 ± 0.1	60.8 ± 0.1	62.5 ± 0.1	65.0 ± 0.1	62.5 ± 0.1	63.7 ± 0.1
Diameter (mm)	29.8 ± 0.1	29.8 ± 0.1	29.8 ± 0.1	29.8 ± 0.1	29.8 ± 0.1	29.6 ± 0.1	29.7 ± 0.1
Porosity (%)	2.42 ± 0.03	2.15 ± 0.09	10.48 ± 0.24	2.57 ± 0.03	25.10 ± 0.05	1.71 ± 0.29	16.60 ± 0.15
Permeability (mD)	-	-	-	-	-	-	-
Pore Volume (mm^3)	1038 ± 22	937 ± 47	4444 ± 140	1120 ± 23	11370 ± 117	735 ± 132	7326 ± 127
Matrix density (g/cm^3)	2.75 ± 0.01	2.75 ± 0.01	2.75 ± 0.01	2.90 ± 0.01	2.77 ± 0.01	2.80 ± 0.01	2.82 ± 0.01
Bulk density (g/cm^3)	2.68 ± 0.02	2.69 ± 0.02	2.47 ± 0.03	2.82 ± 0.02	2.07 ± 0.01	2.76 ± 0.03	2.36 ± 0.02
σ_{diff} (MPa)	45	45	45	45	10	45	10

Table 5. Properties of the core samples used in experimental series D: CCS tests (varying σ_1).

CCS (Vary σ_1)	**Experiment**							
Type	Calcschist	Marble	Limestone	Quartzite	Siltstone	Quartzschist	Mudstone	Micaschist
Code	TD12-CS5	TD1-M4	TS2-SZL4	TD20-QZ-1	TK-B1-2	TD-23-QMS1	TK-B2-1	TD25-MS-1
Length (mm)	61.5 ± 0.1	62.5 ± 0.1	60.8 ± 0.1	62.8 ± 0.1	62.7 ± 0.1	62.5 ± 0.1	63.7 ± 0.1	41.0 ± 0.1
Diameter (mm)	29.8 ± 0.1	29.8 ± 0.1	29.8 ± 0.1	29.8 ± 0.1	29.8 ± 0.1	29.6 ± 0.1	29.7 ± 0.1	29.7 ± 0.1
Porosity (%)	2.42 ± 0.03	2.15 ± 0.09	10.48 ± 0.24	2.77 ± 0.16	22.55 ± 0.01	1.71 ± 0.29	16.60 ± 0.15	8.52 ± 0.37
Permeability (mD)	-	-	-	-	97 ± 6	-	-	-
Pore Volume (mm^3)	1038 ± 22	937 ± 47	4444 ± 140	1213 ± 81	9861 ± 87	735 ± 132	7326 ± 127	2420 ± 128
Matrix density (g/cm^3)	2.75 ± 0.01	2.75 ± 0.01	2.75 ± 0.01	2.89 ± 0.01	2.78 ± 0.01	2.80 ± 0.01	2.82 ± 0.01	2.92 ± 0.01
Bulk density (g/cm^3)	2.68 ± 0.02	2.69 ± 0.02	2.47 ± 0.03	2.81 ± 0.02	2.15 ± 0.01	2.76 ± 0.03	2.36 ± 0.02	2.67 ± 0.02
σ_2 (MPa)	17	17	9	33	12	31	12	31
σ_1 (MPa)	17–40	17–40	9–30	33–70	12–20	31–70	12–17	31–68

In experimental series B (Table 3), σ_1 was set equal to σ_2 at all times. Active-source acoustic measurements were taken at intervals of 5 MPa, until a maximum of 60 MPa was reached. In series C (Table 4), σ_{diff} (i.e., σ_1- σ_2) was kept constant at either 45 or 10 MPa. Due to the relatively weak nature of the silt- and mudstone samples, σ_{diff} was set equal to 10 MPa, instead of 45 MPa, for these specific experiments. Once again, acoustic measurements were performed at 5 MPa intervals, until σ_1 and σ_2 equalled 95 MPa (or 60 MPa for silt- and mudstone samples) and 50 MPa, respectively. Experimental series D (Table 5) reflect the seismic response characterisation at field-representative stress conditions. Here, σ_2 was fixed whereas σ_1 was varied, the latter reflecting different depths within the Kızıldere reservoir. Once more, the active-source acoustic measurements were taken as a function of varying σ_1. Appropriate magnitudes for σ_1 (ranging from 9–70 MPa) and σ_2 (ranging from 9–33 MPa), that prevail at the Kızıldere geothermal field (Table 5), were taken from the literature [35]. For all abovementioned CCS experiments, the axial load was increased at a rate of 0.05 kN/s between two consecutive acoustic measurements.

Although all laboratory measurements were conducted under dry conditions (i.e., dry pore space), one additional test ($\sigma_1 = \sigma_2$) was performed on a previously fractured, still intact, calcschist sample (TD12-CS4 in Table 2) that was (partly) saturated with brine representative of the Kızıldere reservoir. The original reservoir brine composition contains multiple ions in solution such as bicarbonate, carbonate, calcium, magnesium, and potassium. It was decided to mimic the original brine composition using a simplified sodium chloride-based solution equal in total ionic strength.

For several rock types, the same core sample was used for experimental series A–D for comparison purposes, i.e., to eliminate the potential heterogeneity effect amongst different cores from the same rock. Here, first experiment B ($\sigma_1 = \sigma_2$) was conducted followed by C (fixed σ_{diff}), then D (varying σ_1), and finally A (UCS).

All abovementioned UCS and CCS experiments were conducted at ambient temperature (22 ± 1 °C). For all series, A to D, a seismic source was placed at the top of the rock sample whereas a receiver was located at the bottom. For both source and receiver, a single-element normal-incidence shear wave transducer from OLYMPUS was used. The source signal is characterised by a sinus wave with a 1 MHz frequency and an amplitude of 800 mV. A burst period of 5 ms was used and the signal was averaged over a total of 512 shots. One active-source acoustic measurement was taken every 10 s. Figure 2 presents a schematic of the experimental set-ups used for conducting both the UCS and CCS experiments.

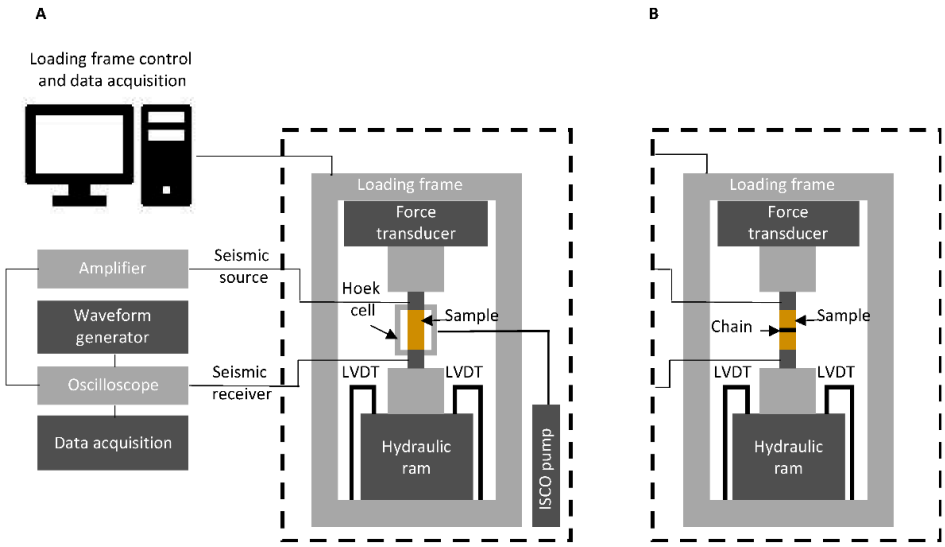

Figure 2. Schematics of the experimental set-ups. Set-up (**A**) was used for conducting CCS experiments while set-up (**B**) was utilised for performing UCS experiments. In order to switch from set-up (**A**) to (**B**), the parts surrounded by dashed lines were substituted.

2.5. Experimental Procedure: Temperature Effect

Besides studying the effect of both σ_1 and σ_2 on the seismic velocity behaviour, the effect of temperature, at σ_1 of 0.069 ± 0.002 MPa and atmospheric pressure, was assessed as well. An overview of the physical properties of the different rock samples used for this purpose is shown in Table 6.

After determining their physical properties, each of the samples presented in Table 6 was placed in an oven at 40 °C for 24 h. Subsequently, the first sample was taken from the oven and positioned in between two metal blocks, providing a σ_1 of 0.069 ± 0.002 MPa. Between the sample and the two blocks two shear-wave transducers, i.e., a seismic source and receiver, were placed. A minimum of three active-source acoustic measurements were taken, using the exact same acoustic settings as was used during the UCS/CCS experiments, yielding a total measurement time of roughly 30 s per sample. Afterwards, the sample was

placed back in the oven and the procedure was repeated for the next sample. As soon as all eight rock samples were tested at 40 °C, the temperature of the oven was set to 60 °C and, consequently, 24 h later the abovementioned process was repeated. This procedure continued until a temperature of 240 °C, representing the current maximum reservoir temperature at Kızıldere, was reached. All acoustic measurements were conducted at σ_2 equal to atmospheric pressure. A fixed temperature interval of 20 °C was used. Figure 3 shows a schematic of the laboratory set-up used for performing the acoustic measurements at varying temperatures.

Table 6. Properties of the core samples used for studying the effect of temperature on seismic velocity.

Temp. Effect	**Experiment**							
Type	Calcschist	Marble	Limestone	Quartzite	Siltstone	Quartzschist	Mudstone	Micaschist
Code	TD12-CS6	TD1-M7	TS2-SZL3	TD20-QZ-3	TK-B1-1	TD-23-QMS2	TK-B2-2	TD25-MS-2
Length (mm)	60.1 ± 0.1	61.3 ± 0.1	60.4 ± 0.1	61.2 ± 0.1	65.0 ± 0.1	61.8 ± 0.1	42.0 ± 0.1	36.1 ± 0.1
Diameter (mm)	29.5 ± 0.1	29.8 ± 0.1	29.0 ± 0.1	29.8 ± 0.1	29.8 ± 0.1	29.6 ± 0.1	29.1 ± 0.1	29.8 ± 0.1
Porosity (%)	3.10 ± 0.16	2.34 ± 0.19	3.97 ± 0.21	4.46 ± 0.10	25.10 ± 0.05	2.99 ± 0.15	17.89 ± 0.17	7.78 ± 0.08
Matrix density (g/cm^3)	2.76 ± 0.01	2.75 ± 0.01	2.72 ± 0.01	2.89 ± 0.01	2.77 ± 0.01	2.84 ± 0.01	2.85 ± 0.01	2.91 ± 0.01
Bulk density (g/cm^3)	2.67 ± 0.02	2.69 ± 0.02	2.61 ± 0.02	2.76 ± 0.03	2.07 ± 0.01	2.75 ± 0.02	2.34 ± 0.03	2.69 ± 0.03
Additional σ_1 (MPa)	0.070 ± 0.001	0.068 ± 0.001	0.072 ± 0.001	0.068 ± 0.001	0.068 ± 0.001	0.069 ± 0.001	0.072 ± 0.001	0.068 ± 0.001
Temperature (°C)	40–240	40–240	40–240	40–240	40–240	40–240	40–240	40–240

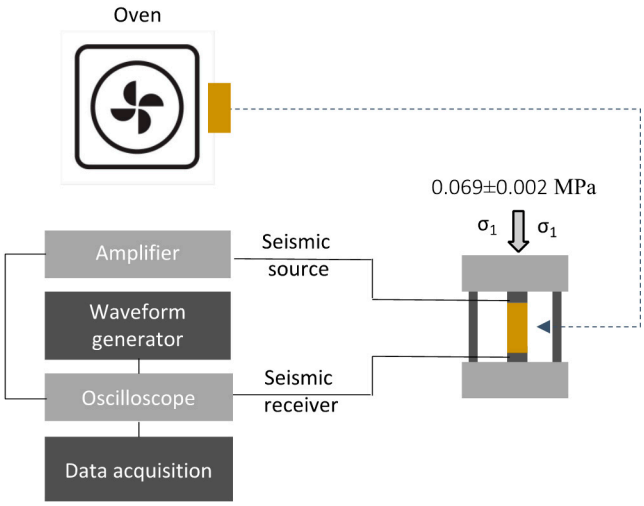

Figure 3. Schematic of the set-up used for assessing the effect of temperature on seismic velocity.

3. Results and Discussion

3.1. Thin Section Analyses

Several rock samples, collected at the Kızıldere site, were shipped for thin section preparation. Table 7 presents the image analyses results and mineralogy obtained from the thin section analyses. The 2D area and perimeter, of the connected pores within an area of interest, were implemented in the 2D Carman-Kozeny equation [37,38] to obtain the presented 2D permeability. Pixel size equals 10 µm × 10 µm. Note that, due to preparation damage and a stress-free matrix, all 2D permeability values shown are likely to be overestimated by at least one order of magnitude. The results indicate that the presence of a fracture increases the 2D permeability by a factor of roughly 10 on average, compared to the matrix permeability only. The latter is in line with the fact that geothermal production in Kızıldere is mainly dependent on fluid flow through fractures [33,36]. The identified mineral composition might shed light on the acoustic behaviour, as a function of stress and temperature, of the various rock types studied.

Table 7. Image analyses results and mineralogy obtained from thin section analyses on several Kızıldere samples. Note that the shown 2D permeability values are overestimated by at least one order of magnitude due to the stress-free matrix and potential preparation damage.

Type	**Calcschist**	**Marble**	**Limestone**	**Micaschist**	**Quartzschist**
Code	TD11-B	TD1-B	TS1-B5	TD24-B	TD23-B
Area porosity (%)	Incl. fracture: 1.3 Excl. fracture: 0.4	Total [d]: 1.6 Effective [d]: 0.4	Effective: 1.5	Total: 8 Effective: 2.3	Incl. fracture: 16.7 Excl. fracture: 10.5
2D Carman-Kozeny permeability (D) Incl. fracture [a] Matrix only [b]	2.5 0.3	2.2 0.1	12.4 -	2.6 -	24.1 5.7
Mineralogy (area%) [c]	-Calcite and dolomite (recrystallised) -Muscovite and sericite -Quartz or feldspar 98 1 <1	-Calcite and dolomite (recrystallised) -Smectite (haloysite?) 99 1	-Calcite and dolomite -Organic matter and oxides 99 1	-Calcite and dolomite (with organic matter) -Angular quartz and feldspar -Smectite (vermiculite?) -Biotite remnants 89 8 2 <1	-Calcite, dolomite and ankerite -Muscovite and sericite -Quartz and feldspar 30 25 45

[a] Permeability shown is related to intergranular pore-connected micro-porosity from up to 100 pixels pores including the rock matrix and fractures (if available). [b] Permeability shown is related to intergranular pore-connected micro-porosity from up to 100 pixels pores, i.e., matrix permeability. [c] Mineral composition is based on random point counting of 100 points in the image texture. [d] Total and effective porosity represent the area of connected and isolated pores and solely connected pores, respectively.

Bulk of the porous media studied showed the presence of fractures. In the calcschist section, a relaxation fracture, filled with muscovite, was identified. The marble sample showed no primary syn-tectonic fractures, though possible secondary fractures within its intergranular space may be present. The limestone texture exhibited a vague brecciated structure, most probably due to the syn-sedimentary fractures present. Moreover, secondary sharp fractures, running mostly through the mud part of its texture, were observed. The micaschist thin section demonstrated the presence of original fractures in the sample matrix filled with clays and organic matter. Additionally, secondary sharp fractures, running typically from the edges, were seen. It is believed that these are most likely preparation induced. The quartzschist sample showed relaxation fractures parallel and angular to the foliation plane.

3.2. Acoustic-Assisted UCS Experiments

Experimental series A, i.e., acoustic-assisted UCS experiments, consists of a total of 14 UCS experiments conducted on different rock types present in the Kızıldere geothermal field (Table 2). Table 8 presents an overview of the static elastic parameters obtained from the UCS experiments. The axial stress–strain relationships for all UCS tests performed are shown in Figure 4.

Table 8. Static elastic parameters obtained from the UCS experiments.

UCS	**Experiment**													
Type	Calcschist		Marble		Limestone				Quartzite		Siltstone		Quartzschist	Mudstone
Code	TD12-CS4	TD12-CS5	TD1-M2	TD1-M3	TS2-SZL2	TS2-SZL4	TS2-SZL5	TD20-QZ-1	TD20-QZ-2 [a]	TD20-QZ-4	TK-B1-2	TK-B1-3	TD-23-QMS1	TK-B2-1
Ultimate strength (MPa)	44.4	45.6	57.0	51.1	145.4	72.5	43.7	82.0	48.3	88.8	15.5	14.5	75.4	22.2
Static Young modulus (GPa)	22.2	26.5	40.1	29.5	52.9	33.9	27.9	35.0	38.5	38.0	3.8	3.8	43.1	10.5
Static Poisson ratio (-)	0.14	0.14	0.17	0.14	0.39	0.19	0.09	0.11	-	0.17	0.27	0.23	0.18	0.16
Bulk modulus (GPa)	10.3	12.3	20.3	13.7	80.2	18.2	11.3	15.0	-	19.2	2.8	2.3	22.4	5.1
Shear modulus (GPa)	9.7	11.6	17.1	12.9	19.0	14.2	12.8	15.8	-	16.2	1.5	1.5	18.3	4.5

[a] During this experiment the extensometer chain, used to monitor the radial strain, failed. Hence, the static Poisson ratio, and indirectly the bulk and shear moduli, could not be obtained.

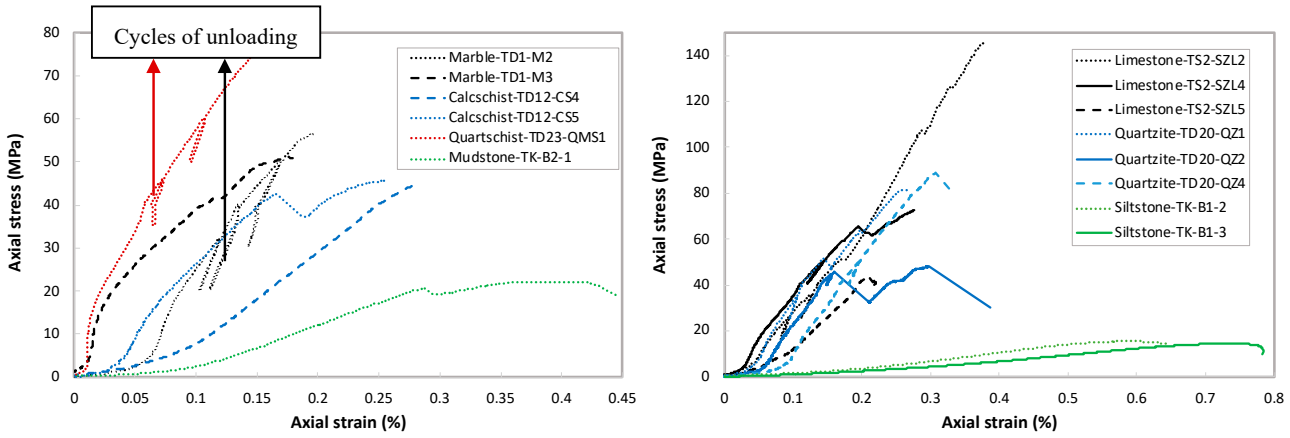

Figure 4. Axial stress–strain behaviour from the 14 UCS experiments performed. For some UCS tests, unloading cycles were also performed. For the limestone samples (black trends in bottom graph): note the variation in ultimate strength and stress–strain slope due to heterogeneity as a result of diagenesis.

The laboratory results clearly indicate that limestone sample TS2-SZL2 is the stiffest material assessed; the steep axial stress–strain slope between 0.2–0.3% strain yields a high Young modulus (E) of 52.9 GPa. On the other hand, it is apparent that the tested siltstone cores are the weakest, i.e., softest, samples studied. The very gentle axial stress–strain slopes (E = 3.8 GPa) suggest that the material underwent a relatively substantial amount of deformation before rock failure occurred.

The steep axial stress-strain trend, at strain values of >0.2%, related to limestone sample TS2-SZL2, suggests that the material experienced relatively little axial deformation prior to failure at σ_1 = 145.4 MPa. This implies a somewhat more brittle-like behaviour of the particular limestone core compared to the other rock samples. The latter is supported by the post-failure fracture pattern observed in the sample (Figure S1 in Supplementary Materials). Figure S1 indicates axial splitting for the limestone and quartzite cores, an indication of brittleness, whereas the other rock samples (marble, calcschist, quartzschist, mudstone, and siltstone) show a clear shear failure pattern. The degree of axial splitting amid the limestone and quartzite cores differs and appears to be related to their porosity: presence of axial splitting patterns increases with decreasing porosity.

The results shown in Table 8 and Figure 4 reveal large variations among the three limestone samples assessed. Though all limestone cores were drilled from the same block, large discrepancies in static elastic parameters are observed. Most probably, a high level of heterogeneity, due to diagenesis processes and the presence of fossils, within the limestone yields different axial stress-strain relationships for the three samples investigated.

Besides studying the elastic properties of the different rock types present at the Kızıldere geothermal site, acoustic measurements were conducted, over the course of each UCS experiment, in order to study the effect of σ_1 on the seismic velocities whilst σ_2 equalled atmospheric pressure. Figure 5 presents the compressional wave (P-wave) velocity as a function of σ_1, i.e., depth below surface. The shear wave (S-wave) velocity as a function of σ_1 is shown in the Supplementary Materials (Figure S2). It is evident from Figure 5 that the soft siltstones reveal significantly lower seismic velocities compared to the other rock types investigated. Since the siltstones underwent a relatively high degree of axial deformation, as previously discussed, compaction within the siltstones occurred, which led directly to an increased seismic velocity as a function of increasing σ_1. For all types of porous media studied, the largest increase in velocity took place at the lowest absolute stress values. This is most likely the result of closure of potential microcracks within the core samples, yielding increased grain-to-grain (or mineral-to-mineral) contact areas, eventually resulting in an increased velocity. Besides the earlier arrival times of the source signal, i.e., higher velocities, the increased contact areas also yield higher amplitude magnitudes (Figure S3 in the Supplementary Materials).

Limestone sample TS2-SZL2 (continuous black line in bottom graph of Figure 5) shows a somewhat different trend compared to the other samples studied: the P-wave velocity remained fairly constant as a function of increasing σ_1. The reason for this is the stiff behaviour of this particular sample (Young Modulus of 52.9 GPa, Table 8): the sample faced relatively little axial deformation with increasing σ_1, yielding negligible amounts of compaction, hence a roughly constant velocity profile.

3.3. Acoustic-Assisted CCS Experiments: $\sigma_1 = \sigma_2$

In Experimental series B (i.e., acoustic-assisted CCS experiments where σ_1 was set equal to σ_2) a total of eight CCS tests were performed on the numerous rock types collected from the Kızıldere site (Table 3). Figure 6 presents the P-wave velocity as a function of increasing $\sigma_1 = \sigma_2$. The S-wave velocity, as a function of increasing $\sigma_1 = \sigma_2$, is shown in Figure S4 (see Supplementary Materials).

Similar to the results of the performed UCS experiments (Section 3.2), the acoustic results shown in Figure 6 also indicate that the largest increase in P-wave velocity occurred at the lowest absolute stress levels. Most probably, as previously discussed, this is a consequence of potential closures of microcracks within the assessed porous media. Once again, the weakest material investigated, i.e., siltstone, reveals the lowest P-wave velocity. In fact, the eight rock types investigated can be classified into the following groups: soft and hard porous media. The soft materials, i.e., micaschist, silt- and mudstone, are characterised by a relatively low bulk density ($\leq 2.67 \pm 0.02$ g/cm^3) and high porosity ($\geq 8.52 \pm 0.37\%$). They reveal relatively low P-wave velocities. The hard materials, with the exception of the limestone, are defined by a high bulk density ($\geq 2.67 \pm 0.02$ g/cm^3) and low porosity

($\leq$2.77 $\pm$ 0.16%). They show high seismic velocities of >4630 m/s for all stresses studied. Furthermore, in line with the observations made in Section 3.2, the limestone sample behaves somewhat differently compared to the other formations: it demonstrates a relatively constant seismic velocity as a function of increasing $\sigma_1 = \sigma_2$. The data points symbolised by circles in Figure 6, representing active-source acoustic measurements during the unloading stage at the end of an experiment, generally follow the loading trend. The latter suggests that the tests were conducted in the elastic regime and no permanent deformation, that might significantly affect the seismic velocity, occurred.

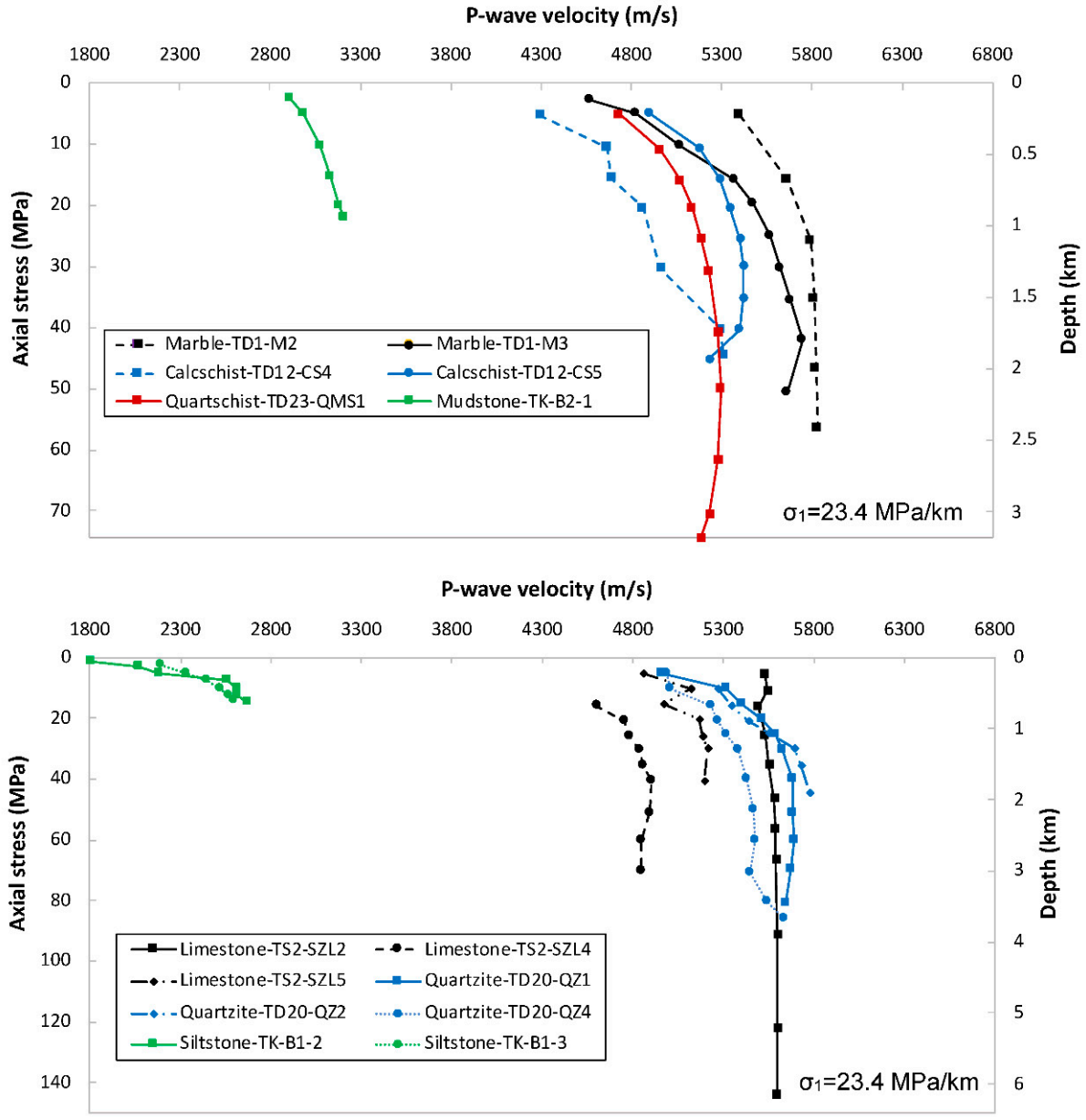

Figure 5. P-wave velocity as a function of axial stress, and thus depth below surface, for all UCS experiments performed. Axial stress–depth relationship is taken from [35].

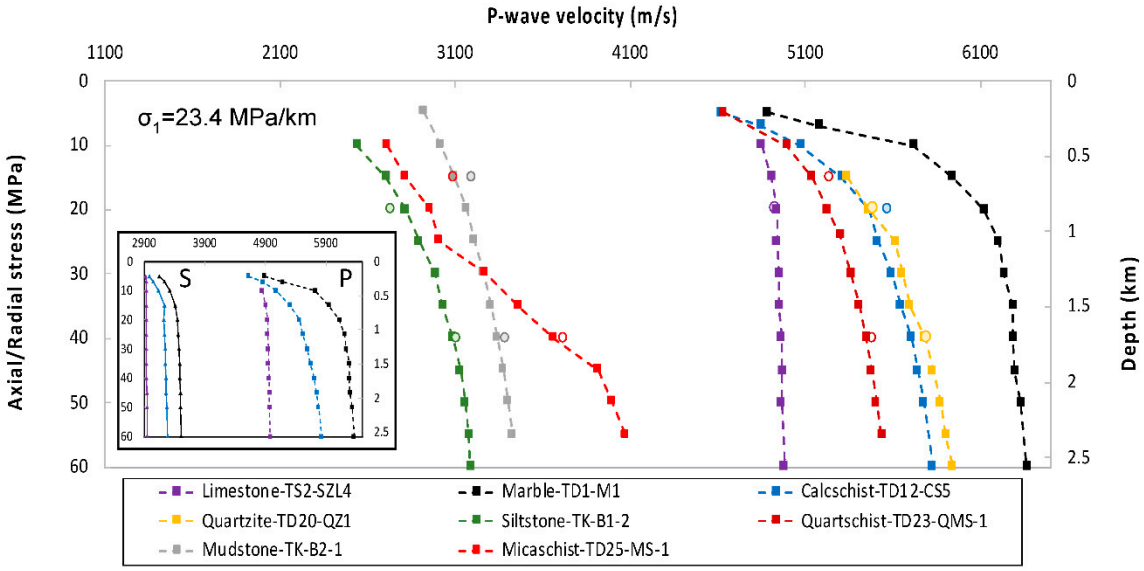

Figure 6. P-wave velocity as a function of axial stress, and thus depth below the surface, for all eight CCS tests conducted within experimental series B. After the samples were loaded until $\sigma_1 = \sigma_2 = 55$–60 MPa (dashed lines), unloading took place during which several acoustic measurements were taken to check for potential hysteresis effects (circular data points). Axial stress–depth relationship is taken from [35]. The graph in the inset presents the P- (dashed lines) and S-wave (continuous lines) velocities for the marble (black), limestone (purple), and calcschist (blue) samples used. Vp/Vs ratios at respectively 10 and 60 MPa of 1.65 and 1.69 (limestone), 1.72 and 1.82 (marble), and 1.62 and 1.77 (calcschist) were found.

3.4. Acoustic-Assisted CCS Experiments: σ_{diff} = Fixed

Experimental series C covers a total of seven CCS experiments where σ_{diff} (i.e., $\sigma_1 - \sigma_2$) was kept constant at 45 MPa (calcschist, marble, limestone, quartzite, and quartzschist) or at 10 MPa (silt- and mudstone). Table 4 presents the physical properties of the various core samples used. Figure 7 shows the P-wave velocity as a function of increasing σ_1 where σ_2 is 45 MPa less than σ_1 (and 10 MPa less for the silt- and mudstone). The S-wave velocity, as a function of increasing σ_1, is shown in Figure S5 (see Supplementary Materials).

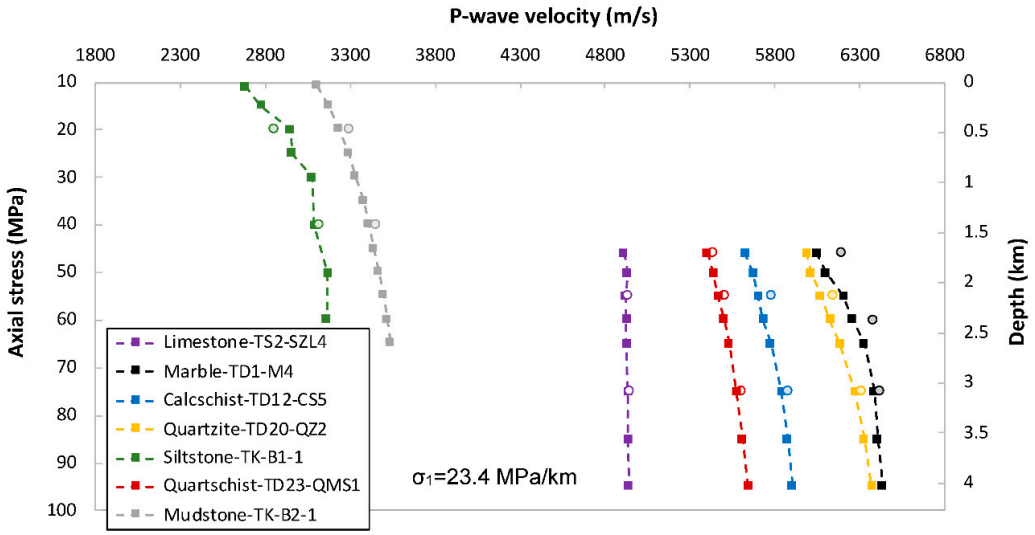

Figure 7. P-wave velocity as a function of axial stress, and thus depth below the surface, for all seven CCS tests conducted within experimental series C. After the samples were loaded until $\sigma_1 = 65$ or 95 MPa (dashed lines), unloading took place during which several acoustic measurements were taken to check for potential hysteresis effects (circular data points). Axial stress–depth relationship is taken from [35].

The laboratory results presented in Figure 7 demonstrate less variation in the P-wave velocity as a function of increasing σ_1 compared to experimental series A (Figure 5) and B (Figure 6). The latter is due to the fact that here the initial measurement was taken at σ_1 = 46 MPa and σ_2 = 1 MPa (except for the silt- and mudstone, as previously mentioned). Due to aforementioned initial conditions, any potential closure of microcracks already occurred prior to reaching σ_1 = 46 MPa. The data in Figure 7 appear to extend the trends shown in Figure 6, except for the quartzite sample. The reason for this might be the fact that another sample, drilled from the same block, was used here compared to experimental series B (Tables 3 and 4).

The same division, i.e., soft and hard materials (discussed in Section 3.3), can be made here as well. The soft silt- and mudstone separate themselves from the other formations by revealing significantly lower seismic velocities. Considering the measurements done during the unloading stage (at the end of an experiment), one may conclude again that the loading process did not permanently alter the internal structure of the rocks that controls its velocity.

3.5. Acoustic-Assisted CCS Experiments: Varying σ_1

A total of eight CCS experiments, where σ_2 was kept constant at its respective field-representative stress, and σ_1 was varied, mimicking the actual depths of the different layers within the Kızıldere geothermal field (Table 5), were performed within experimental series D. Proper magnitudes for σ_1 and σ_2, that occur in the Kızıldere geothermal reservoir (Table 5), were obtained from literature [35]. Figure 8 presents an overview of the obtained P-wave velocities as a function of increasing σ_1. The S-wave velocity as a function of increasing σ_1 is shown in Figure S6 (see Supplementary Materials).

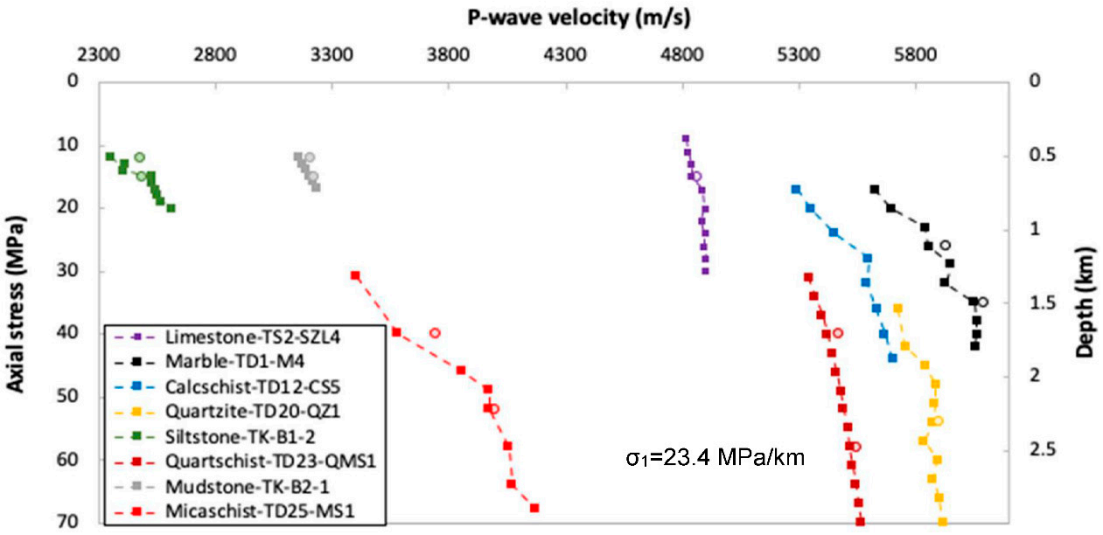

Figure 8. P-wave velocity as a function of axial stress, and thus depth below the surface, for all eight CCS tests conducted within experimental series D. After the samples were loaded until their maximum σ_1 (Table 5), unloading took place during which several acoustic measurements were taken to check for potential hysteresis effects (circular data points). σ_2 was kept constant and is presented in Table 5. Axial stress–depth relationship is taken from [35].

Similar to the observations made for experimental series C (Figure 7), acoustic results related to calcschist, quartzite, quartzschist, micaschist, and marble (Figure 8) show less variation in P-wave velocity, as a function of increasing σ_1, in comparison to the results related to experimental series A (Figure 5) and B (Figure 6). Once again, this is fully related to the initial conditions of the first measurement point at $\sigma_1 = \sigma_2$ of 17, 33, 31, 31, and 17 MPa for the calcschist, quartzite, quartzschist, micaschist, and marble, respectively (Table 5). The latter entails that any potential closure of microcracks, leading to an increased grain-to-grain (or mineral-to-mineral) contact area and thus seismic velocity, already occurred prior

to reaching the abovementioned initial conditions. The loading process, i.e., increasing axial load at a rate of 0.05 kN/s (Section 2.4), seems to take place in the elastic regime as during the unloading cycle similar velocities, that fall well within the loading-related trend, were measured.

Bulk of the data presented in Figure 8 appear to match the acoustic results of experimental series B (Figure 6) relatively well, suggesting a minimal, or negligible, effect of σ_2 on the P-wave velocity. In order to verify this, experiments within series A–D, for which exactly the same core sample was used, are presented in a single plot (Figure 9). From the results, one may conclude that σ_2 appears to have a negligible impact on the P-wave velocity, as long as σ_2 is higher than atmospheric pressure. The reasons for the latter statement are the deviating trends related to the UCS tests, i.e., experimental series A, for quartzite, quartzschist, limestone, and calcschist (Figure 9). Abovementioned UCS-related results indicate lower velocities compared to the case with a confining pressure, i.e., with σ_2 (CCS experiments). This is most likely due to the fact that in the CCS experiments (experimental series B–D) overall compaction was more efficient since it also took place in the radial direction (promoting an increased mineral-to-mineral contact area), as a result of the imposed σ_2, whereas in the UCS experiments (experimental series A) it only occurred in the axial direction. Note that all CCS-related data follow more or less the same trend for each individual rock type investigated.

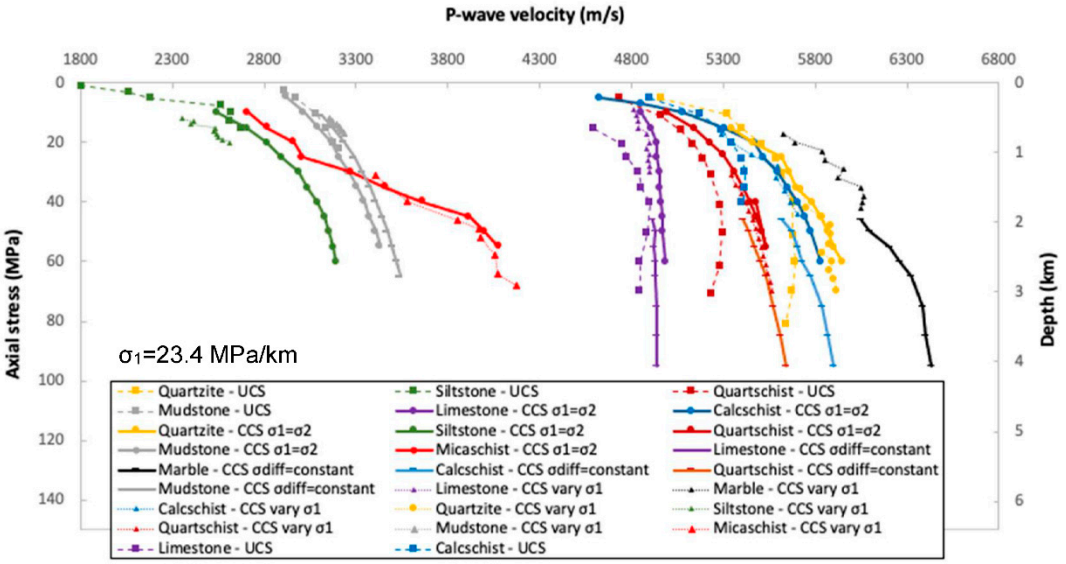

Figure 9. P-wave velocity as a function of axial stress, and thus depth below the surface, for all experiments within series A (UCS), B ($\sigma_1 = \sigma_2$), C (σ_{diff} = constant), and D (vary σ_1), where the exact same core sample was used. Axial stress–depth relationship is taken from [35].

3.6. Acoustic-Assisted CCS Experiments: Effect of Brine-Saturated Pore Space

All laboratory results presented so far are related to dry conditions, i.e., pore space solely filled with air. One additional CCS test, where $\sigma_1 = \sigma_2$ and thus similar to experimental series B (Section 3.3), was carried out for a brine-saturated post-failure calcschist sample (TD12-CS4 in Table 2). A simplified NaCl-based brine, that corresponds to a total ionic strength equal to the total ionic strength of the geothermal water in the Kızıldere reservoir, was prepared. The brine contains 0.41 weight percent (wt%) NaCl. The fractured calcschist sample was saturated by placing it in a glass beaker filled with brine, under vacuum conditions, for more than 15 h. Afterwards, by measuring its wet weight and using the known dry weight, the water saturation was estimated. Table 9 presents an overview of the core properties.

Table 9. Properties of the calcschist sample used to study the effect of a brine-saturated pore space on the seismic velocity. Note that the core sample used here was previously used in experimental series A (Table 2).

CCS ($\sigma_1 = \sigma_2$) Brine-Saturated vs. Dry	**Experiment**	
Type	Calcschist	Calcschist
Code	TD12-CS4	TD12-CS4
Pore fluid	Air (dry)	Brine
Length (mm)	61.5 ± 0.1	61.5 ± 0.1
Diameter (mm)	30.1 ± 0.1	30.1 ± 0.1
Porosity (%)	5.93 ± 0.10	5.93 ± 0.10
Pore Volume (mm^3)	2595 ± 66	2595 ± 66
Matrix density (g/cm^3)	2.78 ± 0.01	2.78 ± 0.01
Bulk density (g/cm^3)	2.62 ± 0.02	2.63 ± 0.02
Water saturation (%)	0	25 ± 2
$\sigma_1 = \sigma_2$ (MPa)	10–50	10–50

Prior to discussing the acoustic results, it is instructive to analyse the formed fracture network in the calcschist sample as a result of the performed UCS test (Section 3.2). Figure 10 presents several cross-sections of the post-failure calcschist sample, obtained with X-ray micro-tomography (micro-CT). The images clearly indicate the presence of a relatively dense fracture network in the upper part of the core sample (cross-sections 1 and 2). The dense network consists of multiple fractures with maximum apertures of around 0.1–0.2 mm or smaller. Moving towards the centre part of the calcschist core (cross-sections 3 and 4), the relatively dense network makes place for a localised shear plane in the form of two connected fractures with a maximum aperture of roughly 0.5 mm (red circle in cross-section 3). Near the bottom part of the core (cross-section 5), the two previously connected fractures became disconnected. A network of fractures, as shown in Figure 10, enhances a reservoir's porosity and permeability, and is crucial for the productivity of the Kızıldere geothermal reservoir (Section 2.1).

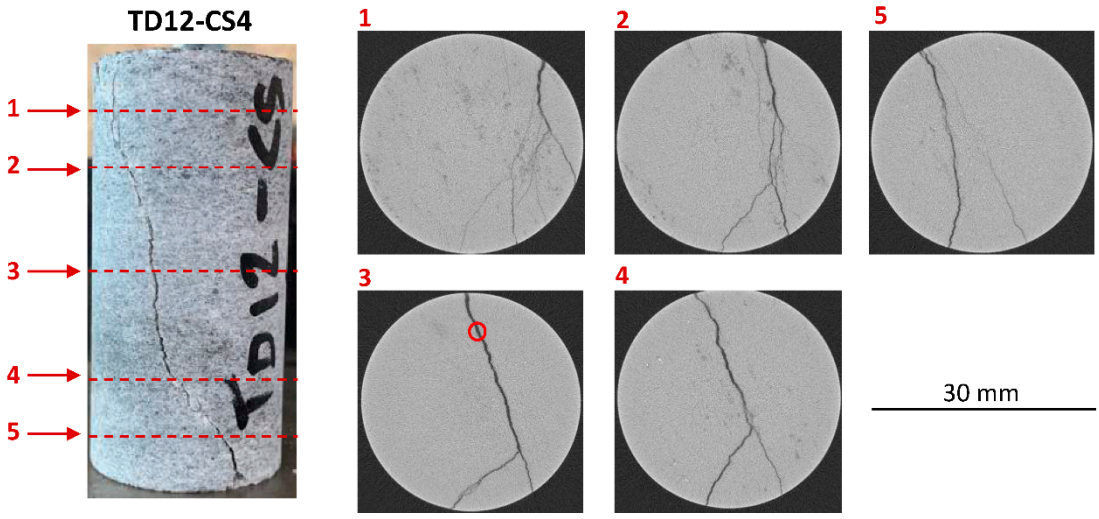

Figure 10. Summary of the fracture network in calcschist sample TD12-CS4. Fractures were formed as a result of the UCS experiment conducted (Section 3.2). Cross-sections 1–5 were obtained with micro-CT scanning using an X-ray tube with 160 kV voltage and a current of 240 µA. Pixel size and slice thickness equals 0.06 × 0.06 and 0.03 mm, respectively. It yields a resolution of 16.67 pixels per mm. The single scan taken consists of a total of 2054 slices, capturing the entire sample length. The maximum observed fracture aperture equals approximately 0.5 mm (red circle in cross-section 3).

Figure 11 presents the seismic velocities, as a function of increasing σ_1 (which equals σ_2), related to the dry- and wet-case experiments as shown in Table 9. Moreover, the acoustic results corresponding to calcschist sample TD12-CS5 in experimental series B (Table 3) are shown as well. Firstly, the effect of a brine-saturated pore space on the seismic velocities will be discussed by comparing the wet-case with the dry-case; both for sample TD12-CS4. Subsequently, an attempt will be made to qualitatively assess the effect of the fracture network in sample TD12-CS4 (Figure 10) on the seismic velocities by comparing its acoustic results with the results obtained for the intact calcschist sample TD12-CS5.

For the S-waves, the data related to the dry- and wet-case (TD12-CS4) are almost identical. This is due to the fact that S-waves cannot propagate in fluids, hence the similar velocities observed in both scenarios. On the contrary, a distinct difference, between the dry- and wet-case, is observed for the P-wave velocity. Since P-waves are able to propagate in fluids, and they travel much faster through water compared to air, it is anticipated that the wet-case would show higher velocities compared to the dry-case, for the investigated stress conditions. An attempt was made to reproduce the wet-case results utilising Gassmann's theoretical framework for fluid substitution [40]. Unfortunately, it appears that Gassmann's methodology is unable to replicate the experimental observations made (Figure 11) as it significantly underestimates the wet-case velocity. Most likely, this is due to Gassmann's assumptions (such as a homogeneous, elastic, and isotropic media and a well-connected pore space) since all of these are not applicable to the calcschist sample studied here.

By comparing the velocities, related to dry conditions, of TD12-CS4 with the results of TD12-CS5, one may qualify the effect of a fracture network (Figure 10) on the resulting velocities. For both the P- and S-wave velocities, the intact sample TD12-CS5 shows significantly higher velocities compared to the fractured sample TD12-CS4 at $\sigma_1 = \sigma_2 \leq 25$ MPa. This is due to the available pore space, i.e., porosity. While the fractured TD12-CS4 shows a porosity of 5.93 ± 0.10 (Table 9), TD12-CS5 reveals a porosity of 2.42 ± 0.03 (Table 3), both at atmospheric conditions. This difference in available pore space yields a lower bulk density of TD12-CS4 compared to TD12-CS5, resulting in lower velocities at $\sigma_1 = \sigma_2 \leq 25$ MPa. For stresses of ≥ 25 MPa, both samples show roughly identical results in terms of velocities. It appears that most of the cracks present in TD12-CS4 have closed at these elevated stress conditions, leading to similar velocities being observed for both calcschist samples. The comparable velocities are a result of both calcschist samples showing similar elastic properties (Table 8) and densities (Table 2) when intact.

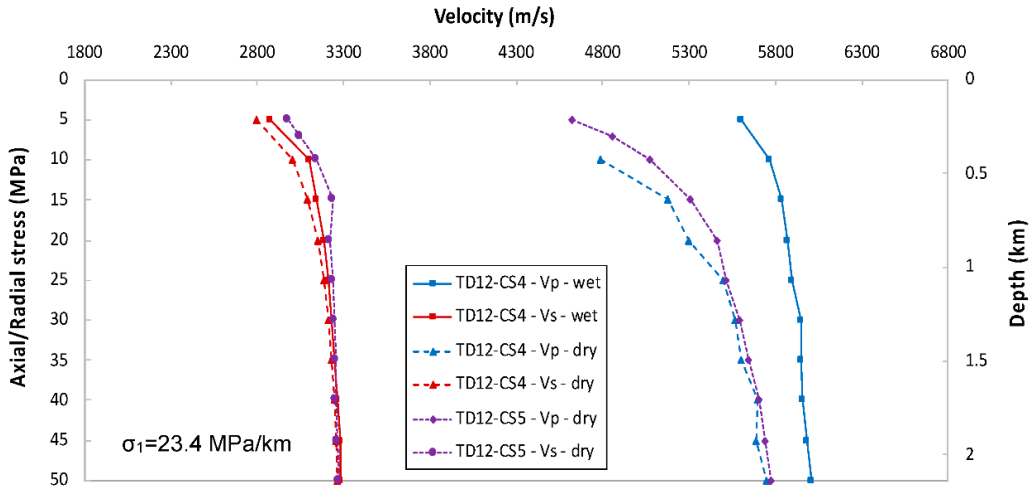

Figure 11. P-wave (blue) and S-wave (red) velocity as a function of axial stress, and thus depth below the surface, for a dry and wet ($25 \pm 2\%$ brine) fractured calcschist sample (TD12-CS4). For comparison purposes, results related to intact calcschist sample TD12-CS5 (from experimental series B) are shown as well (purple). Axial stress–depth relationship is taken from [35].

3.7. Temperature Effect

Aside from investigating the effect of both σ_1 and σ_2 on the seismic velocity, the effect of temperature was studied as well (Table 6 and Figure 3). Experimental conditions include a σ_1 of 0.069 $\pm$ 0.002 MPa and a σ_2 equal to atmospheric pressure. Figure 12 presents the P-wave velocity as a function of increasing temperature for the limestone, marble, and calcschist samples studied. The temperature-P-wave velocity relationships for the other rock types are shown in Figure S7 (see Supplementary Materials). Figures S8 and S9, shown in the Supplementary Materials, present the temperature-dependence of the S-wave velocity.

Most of the rock samples studied (Table 6) reveal reducing P-wave velocities as a function of increasing temperature, with the exception of the mud- and siltstone samples. The latter two porous media disclose a roughly constant velocity with increasing temperature. The reducing velocities, with increasing temperature, were expected and are related to the thermal expansion of the constituting minerals, leading to loosening of the rock's internal structure [28,29,41,42]. Consequently, the mineral-to-mineral contact area reduces, lowering the bulk density, and finally resulting in lower P-wave velocities.

Of the investigated samples, the marble and calcschist cores show the largest decrease in P-wave velocity as a function of increasing temperature (40–240 °C): 42% (marble) and 36% (calcschist). In order to explain this observation, one has to think in terms of thermal expansion coefficients of the comprising minerals. Table 7 shows that the calcschist and marble contain 98% and 99% fully recrystallized calcite and dolomite minerals, respectively. From the literature it is known that calcite minerals possess relatively high thermal expansion coefficients, parallel to the crystallographic c-axis, of 24–29 $\times$ 10^{-6} K^{-1} [42–44]. A study aiming at calcitic and dolomitic marbles from Andalusia (Spain) reported averaged linear thermal expansion coefficients, measured between 20–90 °C, of 11 $\times$ 10^{-6} K^{-1} for both types of marbles [43]. On average, these are somewhat higher than reported mean expansion coefficients, assessed in a range of 20–100 °C, for sandstones and limestones of 10 and 8 $\times$ 10^{-6} K^{-1}, respectively [45]. It is most likely that the thermal expansion coefficients, related to calcite and dolomite minerals, resulted in the overall large drop in velocity, with increasing temperature, observed for the marble and calcschist samples in this study.

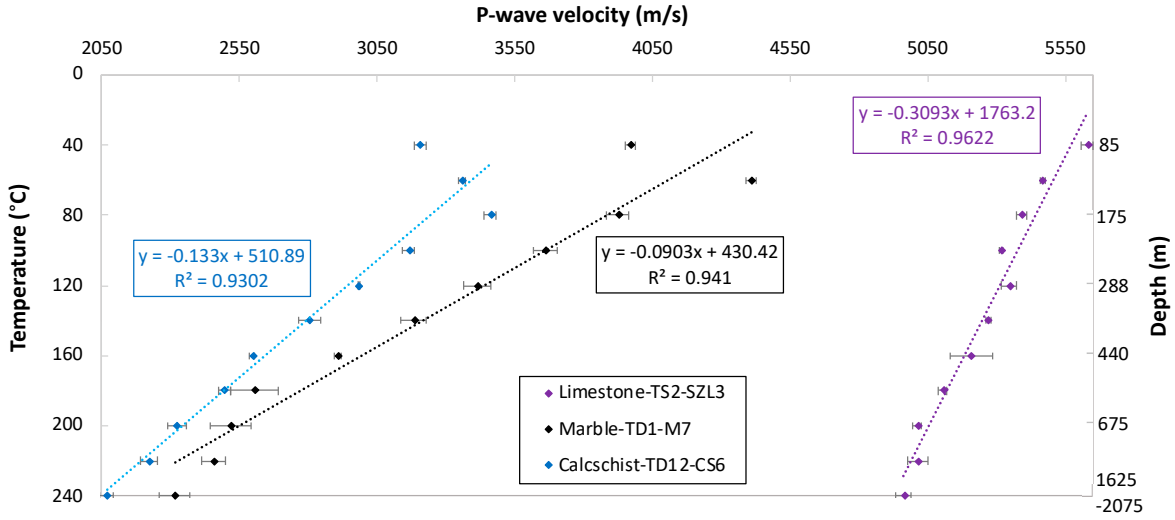

Figure 12. P-wave velocity as a function of temperature (°C), and thus depth below the surface, for the limestone (purple), marble (black), and calcschist (blue) samples assessed. For all three experiments, a linear regression has been applied to the data. A total of three to five measurements were taken every 20 °C. The error bars shown represent the standard deviation, whereas the actual data points denote the averaged seismic velocity. Non-linear temperature–depth relationship is taken from [36].

4. General Discussion

In this section, the results presented in this manuscript will be viewed from the perspective of previous studies. The findings, and related experimental implications, will be examined in the broadest framework possible. Additionally, recommendations for future research will be highlighted.

4.1. Comparison with Observations from the Literature

This study presented a comprehensive experimental investigation into the effects of both σ_1 and σ_2 on the P- and S-wave velocities for a wide range of sedimentary and metamorphic rocks present at the Kızıldere geothermal site. In this subsection, laboratory results obtained for limestone sample TS2-SZL4, in experimental series A (UCS) and B (CCS with $\sigma_1 = \sigma_2$), and acoustic results related to calcschist sample TD12-CS5 (where $\sigma_1 = \sigma_2$; experimental series B) are compared with data from the literature.

Figure 13 shows the P-wave velocity as a function of increasing $\sigma_1 = \sigma_2$ for the calcschist and limestone samples assessed in this study (Table 3), and for two limestone [46,47] and one calcschist [29] samples investigated by other researchers. The calcschist sample studied in [29] is part of the Mandanici Unit from the Peloritani mountain belt in Northern Sicily, Italy. Its mineralogy is heavily dominated by coarse-grained calcite minerals (~71%) and to a lesser extent by quartz (~16%). The limestone investigated in [46] is characterised by a porosity of 13% (mainly consisting of voids or large pores: a vuggy limestone) and by a mineralogy that is greatly dominated by calcite and dolomite minerals. The limestone sample assessed in [47] was sourced from the Molasse Basin, located at the northern front of the Alps, and is part of the Kimmeridgian Reef Complex (Upper Jurassic). It contains a porosity of 13% and a mineralogy that solely consist of calcite minerals, yielding a matrix density of 2.72 g/cm^3.

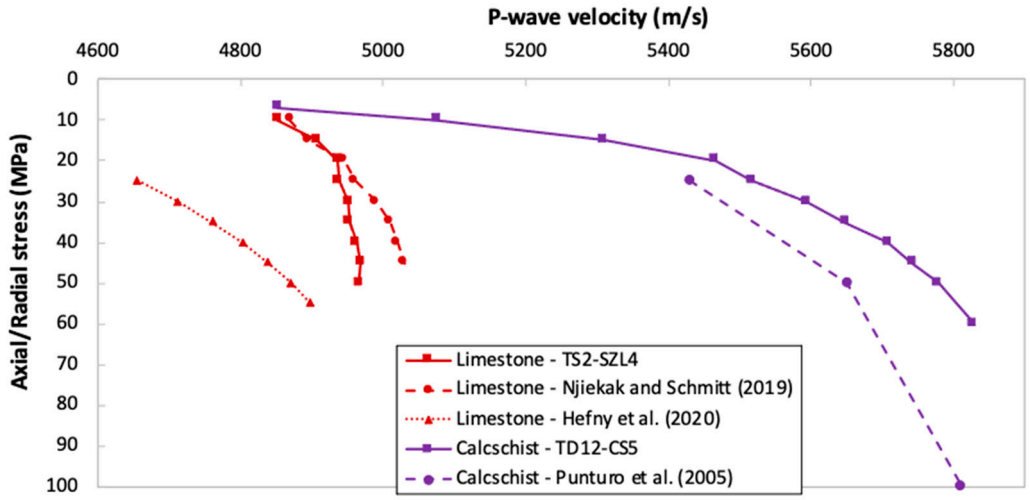

Figure 13. P-wave velocity as a function of axial stress for limestone (TS2-SZL4) and calcschist (TD12-CS5) samples studied in experimental series B (Figure 6). For comparison purposes, acoustic data related to two limestone samples and one calcschist sample were taken from [46,47] and [29], respectively. Experimental conditions involve no differential stress, i.e., axial stress equals radial stress at all times.

The data presented in Figure 13 show that the acoustic-related results for limestone and calcschist, obtained in this study as part of experimental series B, correspond fairly well with the velocity profiles related to one of the two limestones [46] and the calcschist [29] taken from the literature at similar experimental conditions. For the calcschist, the velocities obtained in this study are somewhat higher than the ones reported in [29], nonetheless they follow the same trend. The reason for the difference in absolute velocity might be partly related to its mineralogy. The calcschist samples utilised in this study contain

approximately 98% recrystallized calcite and dolomite minerals (Table 7), whereas the one described in [29] contains also a fair amount of quartz, as mentioned above. Since the P-wave velocity in calcite minerals [48–52] is of a higher magnitude compared to quartz [52–54], this might contribute to the slightly lower calcschist velocities reported in [29].

The presented P-wave velocities corresponding to limestone sample TS2-SZL4 are similar to the ones stated in [46] for $\sigma_1 = \sigma_2 \leq 20$ MPa. For $\sigma_1 = \sigma_2 > 20$ MPa, the limestone sample investigated in this work reveals lower velocities compared to the one studied in [46]. The latter might be related to the amount of compaction, i.e., closure of open pore space, as a function of increasing stress. Since the limestone studied in [46] is characterised by a vuggy porosity, it contains relatively large pores and/or voids. Most probably, these large voids were still not entirely closed at $\sigma_1 = \sigma_2 = 20$ MPa and compaction could continue afterwards, hence its P-wave velocity was able to increase further at $\sigma_1 = \sigma_2 > 20$ MPa. On the other hand, thin section analyses of the limestone sample discussed in this manuscript (Section 3.1) show that its matrix texture contains vugs that are partly filled with secondary crystallised calcite. Assuming that sample TS2-SZL4 contains less, and smaller, voids compared to the limestone reported in [46], most of its open pore space, e.g., voids, may already be closed at $\sigma_1 = \sigma_2 = 20$ MPa. The latter would subsequently lead to a roughly constant P-wave velocity at $\sigma_1 = \sigma_2 > 20$ MPa, as observed in Figure 13.

The limestone sample studied in [47] reveals significantly lower P-wave velocities, as a function of increasing $\sigma_1 = \sigma_2$, compared to sample TS2-SZL4 assessed in this study. Reason for this is most probably the difference in mineral composition. Sample TS2-SZL4 is mainly dominated by calcite and dolomite minerals (Table 7), whereas the limestone investigated in [47] contains calcite minerals only. Calcite minerals reveal P-wave velocities of around 6.26–6.64 km/s [48–52], where dolomite shows velocities of 7.05–7.34 km/s [55,56]. The latter most likely (partly) controls the difference in absolute velocities. The velocity trend of [47] corresponds rather well with the trend observed in [46]. It is related to the open pore space present. As the limestone samples studied in [46,47] both show porosity values of 13%, compaction could continue even after $\sigma_1 = \sigma_2 = 20$ MPa, leading to enhanced mineral-to-mineral contact areas, hence increased P-wave velocities. As mentioned before, for sample TS2-SZL4, bulk of its open pore space might already be closed at $\sigma_1 = \sigma_2 = 20$ MPa, resulting in rather constant velocities with increasing stress.

Figure 14 presents the P-wave velocity-σ_1 relationship for a limestone sample (TS2-SZL4) that was used in this work as part of experimental series A, i.e., the UCS tests (Figure 5). Furthermore, P-wave velocity data for an Indiana limestone, obtained during an UCS experiment, taken from [57] are shown as well (Figure 14). The Indiana limestone reported in [57] is characterised by its homogeneous nature and low strength. Figure 14 shows that the velocities of both limestones are of the same order of magnitude (4500–4900 m/s) and have a very similar trend. The trend consists firstly of a rather rapidly increasing velocity with stress due to compaction. After that, the velocities increase at a slower rate as a function of stress since bulk of the open pore space is already closed, and hence the mineral-to-mineral contact area can only increase slightly. Just before rock failure occurred (at 44.2 MPa for the Indiana limestone and at 72.5 MPa for TS2-SZL4), the P-wave velocity displays a small decrease. This decrease is a result of rock damage, i.e., microcracking [58–61]. The absolute differences in velocity between TS2-SZL4 and the Indiana limestone are related to heterogeneity in terms of rock texture and mineralogy. Where the Indiana limestone is well-known for its relatively homogeneous nature, the limestone samples collected at the Kızıldere site have shown a high level of heterogeneity due to diagenesis processes and the potential presence of fossils (Section 3.2).

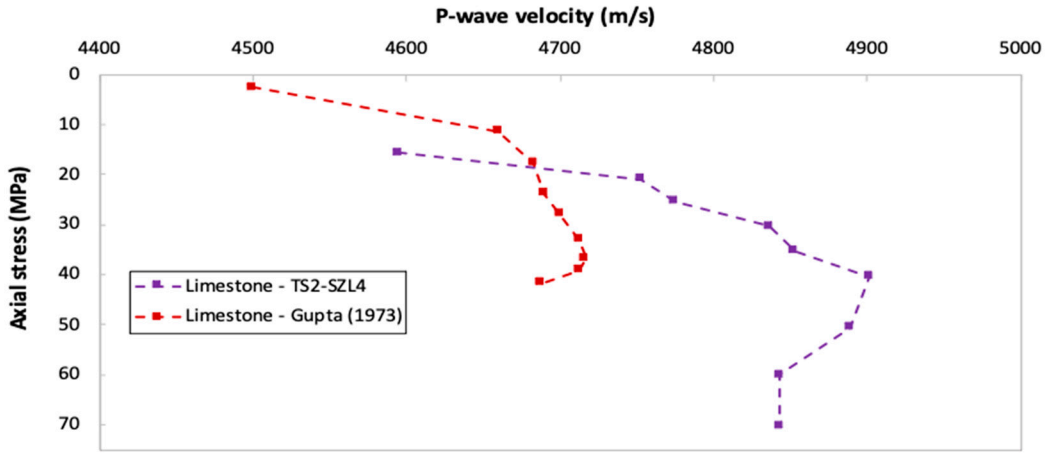

Figure 14. P-wave velocity as a function of axial stress for the limestone sample (TS2-SZL4) used in experimental series A, i.e., the UCS experiments (Figure 5). For comparison purposes, UCS-related acoustic data corresponding to an Indiana limestone sample were taken from [57]. Experimental procedure involves an increasing axial stress until rock failure occurred.

Although absolute velocity values differ between specimens from different regions (Figures 13 and 14), most probably due to variations in mineralogy and microstructure (e.g., pore type and size), the trends in velocities related to the Kızıldere samples seem to broadly correspond to velocity trends observed at other sites. This might imply that there is a potential to use limestone and calcschist velocities, recorded at low stress levels, and extrapolate them to larger stress levels using the observed trends of this study. One crucial parameter to consider in this process is the porosity, i.e., open pore space, as it seems to control the slope of the velocity trend (e.g., limestone samples in Figure 13).

4.2. Experimental Implications and Limitations

As mentioned in Section 2.4, for several rock formations, exactly the same core sample was used for experimental series A–D (Figure 9). This was solely done for comparison purposes, in order to avoid the heterogeneity effect amongst different cores from the same formation. In these cases, first experiment B ($\sigma_1 = \sigma_2$) was conducted followed by C (fixed σ_{diff}), D (varying σ_1), and finally A (UCS). Acoustic-assisted UCS experiments were executed last as these tests resulted in rock failure, making the core sample useless for further testing. One may wonder whether the CCS experiments (series B–D), conducted prior to the UCS test, have altered the internal pore structure of a specific core sample. If the latter is true, the UCS experiments (series A) that followed may not be representative of the initial core sample anymore, thus yielding comparison implications. However, the data points symbolised by circles in Figures 6–8 (i.e., active-source acoustic measurements during the unloading stages) follow quite accurately the observed velocity profiles during loading. This may suggest that the tests were executed in the elastic regime, implying that any deformation, imposed by the elevated stresses, was temporarily and would disappear during the unloading stage. Even if the internal pore structure of the sample slightly changed during the first experiments, comparison among tests conducted on that specific sample might still be preferable over comparing different cores with one another.

Another implication, e.g., source of error, is related to the arrival time picking of the P- and S-waves. Figure 15 presents the active-source acoustic signal obtained during the siltstone TK-B1-3 UCS experiment (series A) at $\sigma_1 = 5.08$ MPa. In order to accurately pick the P-wave arrival time, a horizontal line (black dashed line in Figure 15), representing the maximum noise level in the signal prior to the P-wave arrival, was drawn. The P-wave arrival time was defined as the time at which the signal exceeds this level of maximum noise. In this case this equals 3.433×10^{-5} s, yielding a P-wave velocity of 2333 m/s. Using this methodology, it becomes challenging to quantify the error related to picking P-wave arrival times. In a qualitative way, one can state that the error in picking the P-wave arrival

times is directly proportional to the noise level of the signal. For determining the S-wave arrival times, a somewhat different approach was adopted. Firstly, looking at the complete amplitude spectrum in the time domain, a time frame was identified that corresponds to a significant increase of the signal's amplitude. In the case of Figure 15, this corresponds to 6–8 $\times$ 10^{-5} s. Subsequently, one has to identify the first peak (1 in Figure 15) or trough (2 in Figure 15) that initiates the aforementioned high amplitude time period. Finally, the S-wave arrival time is defined as the time where the signal crosses the background line (i.e., zero amplitude line) just before the significant increase, or decrease, in amplitude. For the case in Figure 15, this resulted in two potential S-wave arrival times of 6.214 and 6.380 $\times$ 10^{-5} s, yielding velocities of 1337 and 1290 m/s, respectively. Thus, the maximum error in picking the S-wave arrival times equalled approximately half a wave period. Throughout this entire study the abovementioned picking procedure was applied in a consistent way, to all rock formations assessed, allowing for mutual comparison.

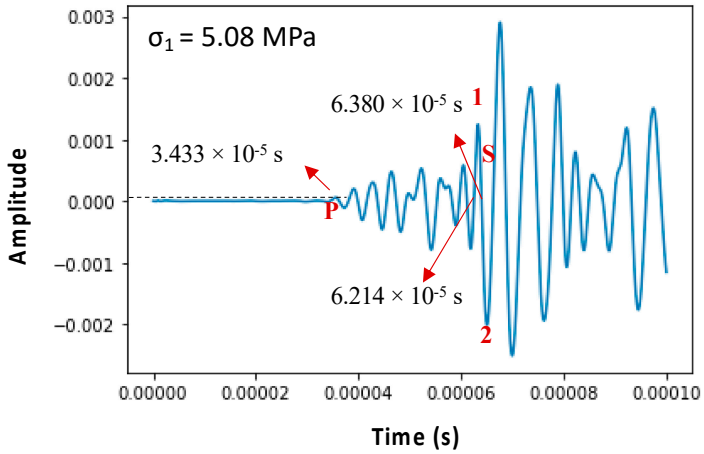

Figure 15. Acoustic signal obtained during the Siltstone TK-B1-3 UCS experiment at σ_1 = 5.08 MPa (Figure 5). Note that the error, related to S-wave arrival time picking, can be interpreted as being equal to ½ wave period.

It is important to note that fracture analyses and characterisation, based on thin section analyses (Section 3.1 and Table 7) and micro-CT scanning (Section 3.6 and Figure 10), was done under atmospheric conditions. Hence, it does not represent properties (e.g., fracture aperture) at subsurface conditions. Stress release, during the unloading phase at the end of the UCS test conducted on calcschist TD12-CS4, presumably affected the detected apertures in Figure 10 [62]. Most probably, at reservoir conditions, the apertures observed in Figure 10 will become smaller due to elevated stress levels.

Finally, in Section 3.7, the effect of increasing temperature on the seismic velocity was investigated. The experimental procedure, as described in Section 2.5, involves placing the samples in the oven for at least 24 h and, subsequently, conducting the active-source acoustic measurement at a room temperature of 22 $\pm$ 1 °C. Though the measurement process for a single sample only took 30 s, within that time frame the rock sample, and especially its surface, cooled down according to Newton's law of cooling [63,64]. When assuming a cooling constant of 7 $\times$ 10^{-3} s^{-1} (based on a heat transfer coefficient of 100 W/m^2/K [65] and a heat capacity of 0.85 J/g/K [66]), in combination with an oven (i.e., initial) temperature of 240 $\pm$ 1 °C, the rock's surface would cool down to approximately 225 and 200 °C after 10 and 30 s, respectively. However, the temperature within the rock itself would most likely still be close to the initial temperature set.

4.3. Velocity Profile of Rocks at the Kızıldere Geothermal Field

The experimental study presented in this manuscript covers an investigation on the stress- and temperature-dependency of seismic velocities for multiple rock types found at

the Kızıldere geothermal field. Considering the results shown in Figure 8 (i.e., velocities at field-representative stress conditions), one may apply linear regression to each individual dataset/rock type. The latter will result in velocity–depth relationships, one per rock type, that are solely stress-dependent and reflect dry conditions. Aforementioned velocity–depth trends can subsequently be applied to any given stratigraphic section, in or around the Kızıldere geothermal site, in order to construct a velocity profile. This was done for a specific stratigraphic section of interest. Corresponding results are presented in Figure 16.

The stratigraphic section shown in Figure 16 represents the planned CO_2 injection location at the Kızıldere geothermal site. The red intervals characterise 'schists' formations. Since it remains questionable to what extend these intervals contain quartz-, calc-, and/or micaschists, a 50% quartzschist and 50% calcschist distribution was assumed, because they yield similar velocities (Figure 8). As it is known that layers of micaschists do occur within the red intervals in Figure 16, potentially serving as local seals within the second reservoir (Table 1), the effect of the addition of micaschists on the resulting velocities was investigated for one single interval. Resulting velocities for the addition of 25, 50, 75, and 100% micaschists (remaining percentage is equally divided between calc- and quartzschist), are shown in blue, green, purple, and red, respectively. Due to its relatively low velocities (Figure 8 and Figure S6), the presence of micaschists will lower the velocity substantially.

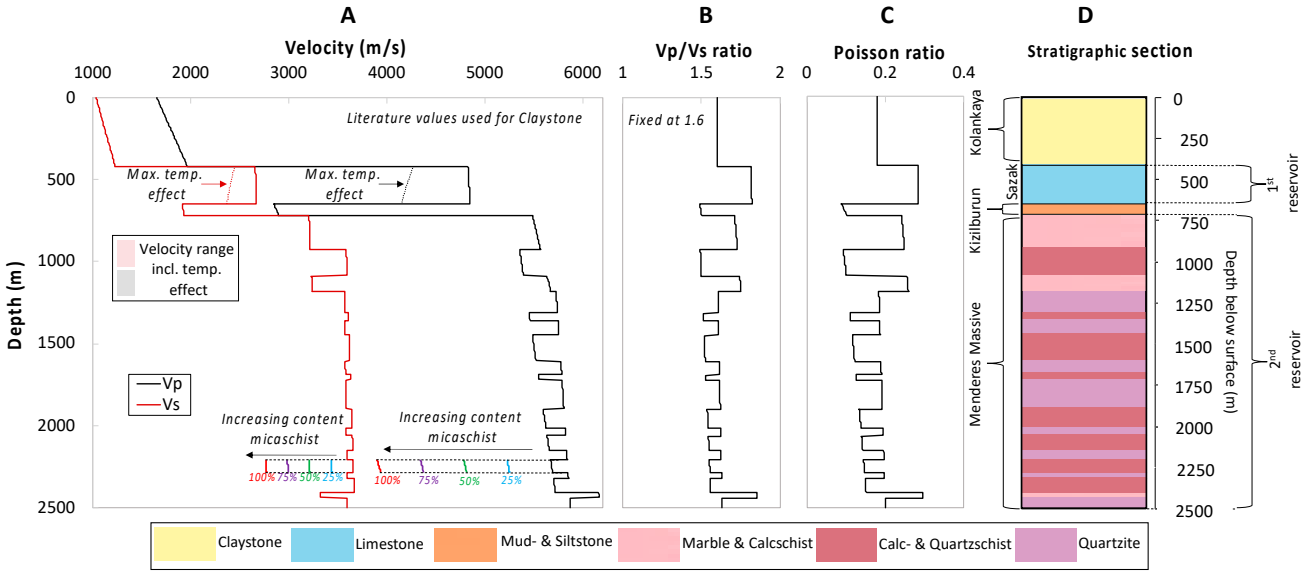

Figure 16. Seismic velocity profiles (**A**), P-wave/S-wave velocity ratio, i.e., Vp/Vs (**B**), Poisson ratio (**C**), and the stratigraphic section of interest (**D**). The stratigraphic section represents the planned CO_2 injection site at the Kızıldere geothermal reservoir. For the intervals that contain multiple rock types (mud- and siltstone, marble and calcschist, and calc- and quartzschist), a 50/50 distribution was assumed. Velocity–depth relationships, i.e., linear regressions, from Figure 8 (P-wave) and Figure S6 (S-wave) were used to construct the profile shown in (**A**). Since the claystone could not be assessed in this study, a literature value for its P-wave velocity, and for its Vp/Vs ratio, was assumed [67]. In one calc- and quartzschist layer, micaschists were added in varying degrees (25, 50, 75, and 100%) to show its effect on the resulting velocities. Note that the velocity profiles presented (black and red profiles in (**A**)) reflect only the stress-dependency of the seismic velocities for dry conditions. In order to give an impression of the effect of temperature, on related velocities, the maximum temperature effect (dashed red and black profiles in (**A**)) was added for the limestone interval. This represents the reduction in velocity with increasing temperature at atmospheric pressure (as presented in Figure 12 and Figure S8). It is expected that the real dry velocity of the limestone interval in (**A**) lies somewhere in between the dashed and continuous lines, as it is assumed that the temperature-dependency is highest at atmospheric conditions, hence the 'maximum temperature effect'.

As mentioned earlier, the velocity profiles presented only reflect the stress-dependency of the seismic velocities for dry conditions. One might wonder to what extend dry conditions are representative of the reservoir. As previously mentioned in Section 2.1., the

geothermal fluid is produced from, and circulates within, the fracture systems. The latter may imply that dry conditions can be found outside of the fracture network, making the velocity profiles presented typical for those areas. Nevertheless, due to the pore fluid effect, the applicability of Figure 16 for the hydrothermal system of the Kızıldere geothermal site is questionable.

The velocity of the P- and S-waves are not solely dependent on stress, but also on temperature, mineral composition, potential presence of cracks and/or voids, etc. Temperature and stress are constantly competing with one another regarding their influence on the velocities. In general, seismic velocities of subsurface rocks reduce with increasing temperature, but tend to show opposite effects due to the substantial increase in stress with increasing depth [68]. However, when approaching the Earth's mantle (10's of km depth), partial melting might occur which may lead to the opposite effect: reducing velocities with depth [68].

For the limestone interval (blue), the maximum temperature effect on the P- and S-wave velocities was added. This reflects the temperature-dependency of the seismic velocities at atmospheric pressure (Figure 12 and Figure S8). Since it is expected that the elevated stress levels in the subsurface will (partly) counteract the thermal expansion (Section 3.7), the effect of temperature on resulting velocities is assumed to be the highest at atmospheric pressure.

4.4. Recommendations and Plans for Future Research

In Section 3.6, the effect of a partly brine-saturated pore space (saturation equalled 25 ± 2%) on the seismic velocity was investigated for post-failure calcschist sample TD12-CS4 (Figure 11). As mentioned previously, an effort was made to replicate the velocities, corresponding to the 25 ± 2% saturation case, using Gassmann's fluid substitution framework [40]. Related results are shown in Figure 17.

It is evident from Figure 17 that Gassmann's concept of fluid substitution [40] significantly underestimates the P-wave velocity for the specific saturated calcschist case. Even with an assumed brine saturation of 100%, the measured velocities could not be approached by the theoretical framework. The reasons for this are most probably the assumptions related to Gassmann's theory. As the concept is derived for, and frequently applied for, fluid estimation, and velocity calculation, from velocities of sandstones (gas versus water bearing), it assumes a fully connected pore space as well as a constant shear modulus. Several researchers observed significant underestimation of the velocity, for carbonate rocks, according to Gassmann's theory [69,70]. For future studies, it is advised to investigate alternative theoretical frameworks for modelling seismic velocities, as a function of pore fluid, for rock formations that do not obey Gassmann's assumptions. An example of an adapted version of Gassmann's theory, derived for carbonates, is presented in [71].

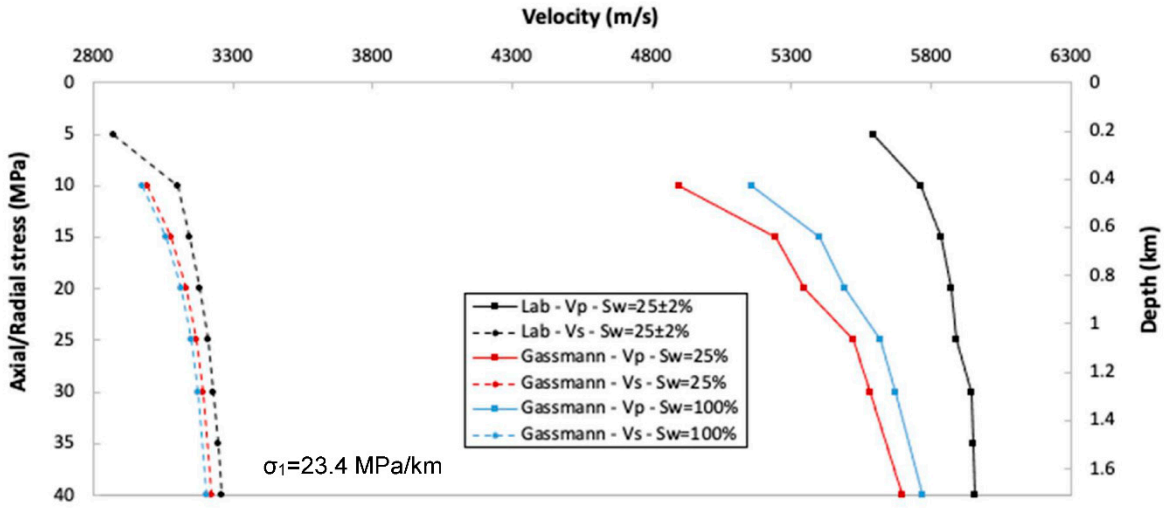

Figure 17. P-wave (continuous lines) and S-wave (dashed lines) velocities as a function of axial stress, and thus depth below the surface, for the (partly) saturated calcschist sample (TD12-CS4) discussed in Section 3.6. Experimental data are shown in black whereas modeled velocities, according to Gassmann fluid substitution [40], for saturations of 25 and 100% are presented in red and blue, respectively. The equations used (Equations (S1) to (S4)), stress-dependent bulk moduli and densities (Table S2), and a short description of Gassmann's fluid substitution is presented in the Supplementary Materials. Axial stress–depth relationship is taken from [35].

All experimental data presented in this manuscript, with the exception of one experiment discussed in Section 3.6, are related to dry pore space conditions. Though it reflects the baseline seismic-response characterisation (Figure 8), one might speculate whether it is representative of real field conditions, as in reality the fractured reservoir rocks in Kızıldere will be (partly) saturated with brine and/or CO_2 due to (re-)injection. Future plans involve large-scale (sample dimensions of 40 × 60 cm; 10 times larger than samples discussed here) acoustic-assisted CCS experiments where the seismic response of altered reservoir rocks, with CO_2/water-saturated flow, will be studied. These large-scale experiments will shed light on the effect of the pore fluid on the resulting velocities; can one, based on the obtained seismic signal, quantify and/or qualify the behaviour of the injected CO_2 in the subsurface?

Besides studying the stress-dependence of the seismic velocity on dry samples, the temperature-dependence, of P- and S-wave velocities, was investigated on dry core samples as well (Section 3.7 and Figure 12), in order to get an initial idea about the temperature effect. In line with previous paragraphs, dry reservoir rocks are not representative of the hydrothermal subsurface conditions at Kızıldere. For future research, it is planned to include a pore fluid for studying the temperature-velocity dependency, at varying stress levels.

5. Conclusions

A laboratory study on the effect of axial (up to 95 MPa) and radial (up to 60 MPa) stress on the seismic velocity was conducted for a broad range of dry sedimentary and metamorphic rocks that are part of the Kızıldere geothermal system. Well-controlled acoustic-assisted unconfined and confined compressive strength experiments yielded the baseline seismic-response characterisation; reflecting the stress-dependence of the seismic velocities. Furthermore, the effect of temperature (up to maximum reservoir temperature of 240 °C), on seismic velocity, at atmospheric pressure conditions, was investigated as well. This study resulted in the following main conclusions:

- Thin section analyses showed that the presence of a fracture increases the 2D permeability by roughly a factor 10 for the main reservoir formations, i.e., marble and

calcschist. This underlines the importance of the presence of fractures in the Kızıldere geothermal reservoir.

- Most of the UCS-related acoustic results showed a similar P-wave velocity–stress trend. It includes a sharp increase in velocity due to initial compaction, followed by a moderate increase in velocity since bulk of the pore space was already closed and, finally, just before rock failure, a slight decrease in velocity due to rock damage (i.e., microcracking).
- Several limestone and quartzite rock samples revealed the presence of axial splitting patterns after failure occurred. The degree of axial splitting appears to be related to their porosity, where the presence of axial splitting fractures increases with decreasing porosity. All marble, calcschist, quartzschist, mudstone, and siltstone samples investigated showed clear shear failure characteristics after rock failure.
- Large variations in static elastic parameters were found among the three limestone samples used for conducting the UCS experiments. Most likely, a high level of heterogeneity, due to diagenesis processes and the presence of fossils, within the limestone yielded different axial stress–strain relationships for the three studied cores.
- Radial stress appeared to have a negligible impact on the P-wave velocity, as long as it was higher than atmospheric pressure. Experiments without any additional radial stress applied on the rock, i.e., UCS experiments, showed lower velocities compared to the experiments where a radial stress was imposed on the sample (CCS experiments). This is due to the fact that in the CCS tests (experimental series B–D), overall compaction was more efficient since it also took place in the radial direction. The latter promoted an increased mineral-to-mineral contact area, hence higher velocities.
- Most of the studied rock formations showed a reducing P-wave velocity as a function of increasing temperature due to thermal expansion of the constituting minerals, leading to loosening of the rock's internal structure. The marble and calcschist samples showed the largest reduction in P-wave velocity as function of increasing temperature (40–240 °C): 42% and 36% for the marble and calcschist samples, respectively.

Supplementary Materials: The following are available online at https://www.mdpi.com/article/10.3390/app11083641/s1, Table S1: List of averaged properties per rock type utilised in this study. Figure S1: Pictures of all 14 rock samples after failure occurred. Note the presence of axial splitting patterns within the limestone (especially TS2-SZL2) and quartzite (mainly TD20-QZ1 and 2) samples. All marble, calcschist, quartzschist, mudstone, and siltstone samples studied reveal clear shear failure characteristics. Figure S2: S-wave velocity as a function of axial stress, and thus depth below surface, for all UCS experiments performed. Axial stress–depth relationship is taken from [35]. Figure S3: Acoustic signal obtained during the Siltstone-TK-B1-3 UCS experiment at σ_1 = 5.08 MPa (left) and 14.02 MPa (right). Besides an earlier arrival time, indicated by the red arrows, at higher stress levels, amplitude magnitudes increased as well (note the different scale of the y-axes). Figure S4: S-wave velocity as a function of axial stress, and thus depth below the surface, for all 8 CCS tests conducted within experimental series B. After the samples were loaded until $\sigma_1 = \sigma_2$ = 55–60 MPa (dashed lines), unloading took place during which several acoustic measurements were taken to check for potential hysteresis effects (circular data points). Axial stress–depth relationship is taken from [35]. Figure S5: S-wave velocity as a function of axial stress, and thus depth below the surface, for all 7 CCS tests conducted within experimental series C. After the samples were loaded to σ_1 = 65 or 95 MPa (dashed lines), unloading took place during which several acoustic measurements were taken to check for potential hysteresis effects (circular data points). Axial stress–depth relationship is taken from [35]. Figure S6: S-wave velocity as a function of axial stress, and thus depth below the surface, for all 8 CCS tests conducted within experimental series D. After the samples were loaded to their maximum σ_1 (Table 5), unloading took place during which several acoustic measurements were taken to check for potential hysteresis effects (circular data points). σ_2 was kept constant and is presented in Table 5. Axial stress–depth relationship is taken from [35]. Figure S7: P-wave velocity as a function of temperature (°C), and thus depth below the surface, for the quartzite (yellow), siltstone (green), quartzschist (dark red), mudstone (grey), and micaschist (red) samples assessed. A total of 3–5 measurements were taken every 20 °C. The error bars shown represent the standard

deviation, whereas the actual data points denote the averaged seismic velocity. Temperature–depth relationship is taken from [36]. Figure S8: S-wave velocity as a function of temperature (°C), and thus depth below the surface, for the limestone (purple), marble (black), and calcschist (blue) samples assessed. For all three experiments, a linear regression has been applied to the data. A total of 3–5 measurements were taken every 20 °C. The error bars shown represent the standard deviation, whereas the actual data points denote the averaged seismic velocity. Temperature–depth relationship is taken from [36]. Figure S9: S-wave velocity as a function of temperature (°C), and thus depth below the surface, for the siltstone (green), mudstone (grey), and micaschist (red) samples assessed. A total of 3–5 measurements were taken every 20 °C. The error bars shown represent the standard deviation, whereas the actual data points denote the averaged seismic velocity. Results related to the quartzite and quartzschist samples are not shown as S-wave arrival was extremely challenging to pick. Temperature–depth relationship is taken from [36]. Table S2: Stress-dependent parameters used in Gassmann's theoretical framework for fluid substitution: bulk moduli and densities for air and brine/water.

Author Contributions: Conceptualization, M.T.G.J., A.B., D.D. and K.-H.A.A.W.; data curation, M.T.G.J.; formal analysis, M.T.G.J., A.B. and K.-H.A.A.W.; funding acquisition, A.B., D.D., K.-H.A.A.W. and S.D.; investigation, M.T.G.J., A.B. and K.-H.A.A.W.; methodology, M.T.G.J., A.B. and K.-H.A.A.W.; project administration, A.B., D.D., K.-H.A.A.W. and S.D.; resources, M.T.G.J.; software, M.T.G.J. and K.-H.A.A.W.; supervision, A.B., D.D. and K.-H.A.A.W.; validation, M.T.G.J.; visualization, M.T.G.J.; writing—original draft, M.T.G.J.; writing—review and editing, M.T.G.J., A.B., D.D., K.-H.A.A.W. and S.D. All authors have read and agreed to the published version of the manuscript.

Funding: This study was carried out within the framework of SUCCEED, which is funded through the ACT programme (Accelerating CCS Technologies, Project No 294766). Financial contributions made by the Department for Business, Energy & Industrial Strategy UK (BEIS), the Rijksdienst voor Ondernemend Nederland (RVO), the Scientific and Technological Research Council of Turkey (TUBITAK), and our research partners Orkuveita Reykjavíkur/Reykjavik Energy Iceland (OR) and Istituto Nazionale di Oceanografia e di Geofisica Sperimentale Italy (OGS) are gratefully acknowledged.

Institutional Review Board Statement: Not applicable.

Informed Consent Statement: Not applicable.

Data Availability Statement: The authors confirm that the processed data, supporting the findings of this study, are available within the article and its Supplementary Materials. Raw data were generated at the Geoscience & Engineering Laboratory of Delft University of Technology and are available from the corresponding author (M.T.G.J.) on request.

Acknowledgments: This study is the first result of a collaboration between Delft University of Technology, Imperial College London, Middle East Technical university (METU), Istituto Nazionale di Oceanografia e di Geofisica Sperimentale (OGS), Silixa Ltd., Seismic Mechatronics, Zorlu Enerji, and Orkuveita Reykjavíkur (OR). Öncü Demircioglu (Zorlu Enerji), Erinç Tonguç (Zorlu Enerji), and Burak Parlaktuna (METU) are gratefully acknowledged for their assistance during the rock sample collection in the region of the Kızıldere geothermal site. We are grateful to Zorlu Enerji for the transportation of the rock samples from Turkey to The Netherlands. The authors thank Marc Friebel (TU Delft), Wim Verwaal (TU Delft), Jens van den Berg (TU Delft), Ellen Meijvogel-de Koning (TU Delft), and Karel Heller (TU Delft) for their technical support.

Conflicts of Interest: The authors declare no conflict of interest. The funders had no role in the design of the study; in the collection, analyses, or interpretation of data; in the writing of the manuscript, or in the decision to publish the results.

References

1. Bertani, B. Geothermal power generation in the world 2010–2014 update report. In Proceedings of the World Geothermal Congress, Melbourne, Australia, 12–24 April 2015.
2. Sanner, B. Summary of EGC 2019 country update reports on geothermal energy in Europe. In Proceedings of the European Geothermal Congress, The Hague, The Netherlands, 11–14 June 2019.

3. Kaygusuz, K.; Guney, M.; Kaygusuz, O. Renewable energy for rural development in Turkey. *J. Eng. Res. Appl. Sci.* **2019**, *8*, 1109–1118.
4. Yamanlar, S.; Korkmaz, E.D.; Serpen, U. Assessment of geothermal power potential in buyuk menderes basin, Turkey. *Geothermics* **2020**, *88*, 101912. [CrossRef]
5. Rybach, L. Geothermal energy: Sustainability and the environment. *Geothermics* **2003**, *32*, 463–470. [CrossRef]
6. Lund, J.W.; Toth, A.N. Direct utilization of geothermal energy 2020 worldwide review. *Geothermics* **2020**, *90*, 101915. [CrossRef]
7. Haklidir, F.S.T.; Baytar, K.; Kekevi, M. Global CO_2 capture and storage methods and a new approach to reduce the emissions of geothermal power plants with high CO_2 emissions: A case study from Turkey. In *Climate Change and Energy Dynamics in the Middle East. Understanding Complex Systems*; Qudrat-Ullah, H., Kayal, A., Eds.; Springer: Cham, Germany, 2019. [CrossRef]
8. Miranda-Barbosa, E.; Sigfússon, B.; Carlsson, J.; Tzimas, E. Advantages from combining CCS with geothermal energy. *Energy Procedia.* **2017**, *114*, 6666–6676. [CrossRef]
9. Pruess, K. Enhanced Geothermal Systems (EGS) using CO_2 as working fluid—A novel approach for generating renewable energy with simultaneous sequestration of carbon. *Geothermics* **2006**, *35*, 351–367. [CrossRef]
10. Xu, T.; Feng, G.; Shi, Y. On Fluid-rock chemical interaction in CO_2-based geothermal systems. *J. Geochem. Explor.* **2014**, *144*, 179–193. [CrossRef]
11. Brown, D.W. A hot dry rock geothermal energy concept utilizing supercritical CO_2 instead of water. In Proceedings of the Twenty-Fifth Workshop on Geothermal Reservoir Engineering, Stanford, CA, USA, 24–26 January 2000.
12. Wolf, K.H.A.A.; Willemsen, A.; Bakker, T.W.; Wever, A.K.T.; Gilding, D.T. The development of a multi-purpose geothermal site in an urban area. In Proceedings of the 70th EAGE Conference and Exhibition Incorporating SPE EUROPEC, Rome, Italy, 9–12 June 2008.
13. Pruess, K. On production behavior of enhanced geothermal systems with CO_2 as working fluid. *Energy Convers. Manag.* **2008**, *49*, 1446–1454. [CrossRef]
14. Salimi, H.; Wolf, K.H.A.A.; Bruining, J. Geothermal energy combined with CO_2 sequestration: An additional benefit. In Proceedings of the 1st ITB Geothermal Workshop, Bandung, Indonesia, 6–8 March 2012.
15. Randolph, J.B.; Saar, M.O. Combining geothermal energy capture with geologic carbon dioxide sequestration. *Geophys. Res. Lett.* **2011**, *38*. [CrossRef]
16. Randolph, J.B.; Saar, M.O. Coupling carbon dioxide sequestration with geothermal energy capture in naturally permeable, porous geologic formations: Implications for CO_2 sequestration. *Energy Procedia.* **2011**, *4*, 2206–2213. [CrossRef]
17. Ezekiel, J.; Ebigbo, A.; Adams, B.M.; Saar, M.O. Combining natural gas recovery and CO_2-based geothermal energy extraction for electric power generation. *Appl. Energy.* **2020**, *269*, 115012. [CrossRef]
18. Cui, G.; Ren, S.; Rui, Z.; Ezekiel, J.; Zhang, L.; Wang, H. The influence of complicated fluid-rock interactions on the geothermal exploitation in the co_2 plume geothermal system. *Appl. Energy.* **2018**, *227*, 49–63. [CrossRef]
19. Adams, B.M.; Kuehn, T.H.; Bielicki, J.M.; Randolph, J.B.; Saar, M.O. A comparison of electric power outlet of CO_2 plume geothermal (CPG) and brine geothermal systems for varying reservoir conditions. *Appl. Energy.* **2015**, *140*, 365–377. [CrossRef]
20. Wyllie, M.R.J.; Gregory, A.R.; Gardner, G.H.F. An experimental investigation of factors affecting elastic wave velocities in porous media. *Geophysics* **1958**, *23*, 459–493. [CrossRef]
21. Prasad, M.; Manghnani, M.H. Effects of pore and differential pressure on compressional wave velocity and quality factor in berea and michigan sandstones. *Geophysics* **1997**, *62*, 1163–1176. [CrossRef]
22. King, M.S. Recent developments in seismic rock physics. *Int. J. Rock Mech. Min. Sci.* **2009**, *46*, 1341–1348. [CrossRef]
23. Darot, M.; Reuschlé, T. Acoustic wave velocity and permeability evolution during pressure cycles on a thermally cracked granite. *Int. J. Rock Mech. Min. Sci.* **2000**, *37*, 1019–1026. [CrossRef]
24. Nur, A.; Simmons, G. The effect of saturation on velocity in low porosity rocks. *Earth Planet. Sci. Lett.* **1969**, *7*, 183–193. [CrossRef]
25. Yu, G.; Vozoff, K.; Durney, D.W. The influence of confining pressure and water saturation on dynamics elastic properties of some permian coals. *Geophysics* **1993**, *58*, 30–38. [CrossRef]
26. He, T.; Schmitt, D.R. Velocity measurements of conglomerates and pressure sensitivity analysis of AVA response. In Proceedings of the 76th SEG International Exposition and Annual Meeting, New Orleans, LA, USA, 1–6 October 2006.
27. Kern, H. The effect of high temperature and high confining pressure on compressional wave velocities in quartz-bearing and quartz-free igneous and metamorphic rocks. *Tectonophysics* **1978**, *44*, 185–203. [CrossRef]
28. Kern, H.; Popp, T.; Gorbatsevich, F.; Zharikov, A.; Lobanov, K.V.; Smirnov, Y.P. Pressure and temperature dependence of vp and vs in rocks from the superdeep well and from surface analogues at kola and the nature of velocity anisotropy. *Tectonophysics* **2001**, *338*, 113–134. [CrossRef]
29. Punturo, R.; Kern, H.; Cirrincione, R.; Mazzoleni, P.; Pezzino, A. P- and S-wave velocities and densities in silicate and calcite rocks from the peloritani mountains sicily (Italy): The effect of pressure, temperature and the direction of wave propagation. *Tectonophysics* **2005**, *409*, 55–72. [CrossRef]
30. Scheu, B.; Kern, H.; Spieler, O.; Dingwell, D.B. Temperature dependence of elastic P- and S-wave velocities in porous mt. *unzen dacite. J. Volcanol. Geoth. Res.* **2006**, *153*, 136–147. [CrossRef]
31. Jaya, M.S.; Shapiro, S.A.; Kristinsdóttir, L.H.; Bruhn, D.; Milsch, H.; Spangenberg, E. Temperature dependence of seismic properties in geothermal rocks at reservoir conditions. *Geothermics* **2010**, *39*, 115–123. [CrossRef]
32. Timur, A. Temperature dependence of compressional and shear wave velocities in rocks. *Geophysics* **1977**, *42*, 950–956. [CrossRef]

33. Halaçoğlu, U.; Fishman, M.; Karaağaç, U.; Harvey, W. Four decades of service—Kızıldere reservoir, units and management. *GRC Transactions* **2018**, *42*.
34. Şimşek, Ş.; Yıldırım, N.; Gülgör, A. Developmental and environmental effects of the kizildere geothermal power project, Turkey. *Geothermics* **2005**, *34*, 234–251. [CrossRef]
35. Çiftçi, N.B. In-Situ stress field and mechanics of fault reactivation in the gediz graben, Western Turkey. *J. Geodyn.* **2013**, *65*, 136–147. [CrossRef]
36. Garg, S.K.; Haizlip, J.; Bloomfield, K.K.; Kindap, A.; Haklidir, F.S.; Guney, A. A numerical model of the kizildere geothermal field, Turkey. In Proceedings of the World Geothermal Congress, Melbourne, Australia, 19–25 April 2015.
37. Carman, P.C. Fluid flow through granular beds. *Trans. Inst. Chem. Eng.* **1937**, *15*, 150–166. [CrossRef]
38. Kozeny, J. Ueber kapillare leitung der wassers im Boden. *Sitzungsber Akad. Wiss. Wien.* **1927**, *136*, 271–306.
39. Hoek, E.; Franklin, J. Simple triaxial cell for field or laboratory testing of rock. *Trans. Inst. Min. Metall.* **1968**, *77*, A22–A26.
40. Gassmann, F. Elastic waves through a packing of spheres. *Geophysics* **1951**, *16*, 673–685. [CrossRef]
41. Fredrich, J.T.; Wong, T.F. Micromechanics of thermally induced cracking in three crustal rocks. *J. Geophys. Res.* **1986**, *91*, 12743–12764. [CrossRef]
42. Weiss, T.; Siegesmund, S.; Kirchner, D.T.; Sippel, J. Insolation weathering and hygric dilatation: Two competitive factors in stone degradation. *Environ. Geol.* **2004**, *46*, 402–413. [CrossRef]
43. Luque, A.; Leiss, B.; Alvarez-Lloret, P.; Cultrone, G.; Siegesmund, S.; Sebastian, E.; Cardell, C. Potential thermal expansion of calcitic and dolomitic marbles from andalusia (Spain). *J. Appl. Crystallogr.* **2011**, *44*, 1227–1237. [CrossRef]
44. Johnson, W.H.; Parsons, W.H. *Thermal Expansion of Concrete Aggregate Materials*; US Government Printing Office: Washington, DC, USA, 1944.
45. Griffith, J.H. Thermal expansion of typical american rocks. *Iowa Eng. Exp. Sta. Bul.* **1936**, *128*, 36.
46. Njiekak, G.; Schmitt, D.R. Effective stress coefficient for seismic velocities in carbonate rocks: Effects of pore characteristics and fluid types. *Pure Appl. Geophys.* **2019**, *176*, 1467–1485. [CrossRef]
47. Hefny, M.; Zappone, A.; Makhloufi, Y.; de Haller, A.; Moscariello, A. A laboratory approach for the calibration of seismic data in the western part of the swiss molasse basin: The case history of well Humilly-2 (France) in the Geneva area. *Swiss J. Geosci.* **2020**, *113*, 11. [CrossRef]
48. Simmons, G. *Single Crystal Elastic Constants and Calculated Aggregate Properties. Report*; Southern Methodist University Press: Dallas, TX, USA, 1965.
49. Bhimasenachar, J. Elastic constants of calcite and sodium nitrate. *Proc. Indian Acad. Sci.* **1945**, *22*, 199–208. [CrossRef]
50. Peselnick, L.; Robie, R.A. Elastic constants of calcite. *J. Appl. Phys.* **1962**, *33*, 2889–2892. [CrossRef]
51. Dandekar, D.P. Pressure dependence of the elastic constants of calcite. *Phys. Rev.* **1968**, *172*, 873. [CrossRef]
52. Anderson, O.L.; Liebermann, R.C. *Sound Velocities in Rocks and Minerals. Report, VESIAC State-of-the-Art Report No. 7885–4-x*; University of Michigan: Ann Arbor, MI, USA, 1966.
53. Sowers, T.; Boyd, O.S. *Petrologic and Mineral Physics Database for use with the US Geological Survey National Crustal Model (No. 2019-1035)*; US Geological Survey: Reston, GA, USA, 2019.
54. McSkimin, H.; Andreatch, P., Jr.; Thurston, R. Elastic moduli of quartz versus hydrostatic pressure at 25 and −195.8 °C. *J. Appl. Phys.* **1965**, *36*, 1624–1632. [CrossRef]
55. Humbert, P.; Plicque, F. Propriétés élastiques de carbonates rhomboédriques monocristallins: Calcite, magnésite, dolomite. *CR Acad. Sci. Paris* **1972**, *275*, 291–304.
56. Nur, A.; Simmons, G. The effect of viscosity of a fluid phase on velocity in low porosity rocks. *Earth Planet. Sci. Lett.* **1969**, *7*, 99–108. [CrossRef]
57. Gupta, I.N. Seismic velocities in rock subjected to axial loading up to shear fracture. *J. Geophys. Res.* **1973**, *78*, 6936–6942. [CrossRef]
58. Pellet, F.L.; Fabre, G. Damage evaluation with P-wave velocity measurements during uniaxial compression tests on argillaceous rocks. *Int. J. Geomech.* **2007**, *7*, 431–436. [CrossRef]
59. Barnhoorn, A.; Cox, S.F.; Robinson, D.J.; Senden, T. Stress- and fluid-driven failure during fracture array growth: Implications for coupled deformation and fluid flow in the crust. *Geology* **2010**, *38*, 779–782. [CrossRef]
60. Barnhoorn, A.; Verheij, J.; Frehner, M.; Zhubayev, A.; Houben, M. Experimental identification of the transition from elasticity to inelasticity from ultrasonic attenuation analyses and the onset of inelasticity. *Geophysics* **2018**, *83*, MR221–MR229. [CrossRef]
61. Bonnelye, A.; Schubnel, A.; David, C.; Henry, P.; Guglielmi, Y.; Gout, C.; Fauchille, A.L.; Dick, P. Elastic wave velocity evolution of shales deformed under uppermost crustal conditions. *J. Geophys. Res.* **2017**, *122*, 130–141. [CrossRef]
62. Wennberg, O.P.; Wall, B.G.; Saether, E.; Jounoud, S.; Rozhko, A.; Naumann, M. Fractures in chalks and marls of the shetland group in the gullfaks field, North Sea. In Proceedings of the 80th EAGE Conference and Exhibition, Copenhagen, Denmark, 11–14 June 2018.
63. Bohren, C.F. Comment on "Newton's law of cooling—A critical assessment" by Colm T. O'Sullivan. *Am. J. Phys.* **1991**, *59*, 1044–1046. [CrossRef]
64. O'Sullivan, C.T. Newton's law of cooling—A critical assessment. *Am. J. Phys.* **1990**, *58*, 956–960. [CrossRef]
65. Kim, K.; Kemeny, J.; Nickerson, M. Effect of rapid thermal cooling on mechanical rock properties. *Rock Mech. Rock Eng.* **2014**, *47*, 2005–2019. [CrossRef]

66. Merriman, J.D.; Hofmeister, A.M.; Roy, D.J.; Whittington, A.G. Temperature-dependent thermal transport properties of carbonate minerals and rocks. *Geosphere* **2018**, *14*, 1961–1987. [CrossRef]
67. Dalfsen, W.V.; Mijnlieff, H.F.; Simmelink, H.J. Interval velocities of a triassic claystone: Key to burial history and velocity modelling. In Proceedings of the 67th EAGE Conference and Exhibition, Madrid, Spain, 13–16 June 2005.
68. Sain, K. Seismic velocity-temperature relationships. In *Encyclopedia of Solid Earth Geophysics. Encyclopedia of Earth Sciences Series*; Gupta, H.K., Ed.; Springer: Dordrecht, The Netherlands, 2011. [CrossRef]
69. Baechle, G.; Weger, R.; Eberli, G.; Massaferro, J.; Sun, Y.F. Changes of shear moduli in carbonate rocks: Implications for gassmann applicability. *Lead. Edge* **2005**, *24*, 507–510. [CrossRef]
70. Baechle, G.; Eberli, G.; Weger, R.; Massaferro, J. Changes in dynamic shear moduli of carbonate rocks with fluid substitution. *Geophysics* **2009**, *74*, E135–E147. [CrossRef]
71. Gegenhuber, N. Application of gassmann's equation for laboratory data from carbonates from Austria. *Austrian J. Earth Sci.* **2015**, *108*, 239–244. [CrossRef]